


Thermal activation barriers for creation and annihilation of magnetic droplet solitons in the presence of spin transfer torque

Gabriel D. Chaves-O'Flynn 

Institute of Molecular Physics, Polish Academy of Sciences, ul. Mariana Smoluchowskiego 17, 60-179 Poznań, Poland

D. L. Stein

Department of Physics and Courant Institute of Mathematical Sciences, New York University, New York, New York 10012, USA; NYU-ECNU Institutes of Physics and Mathematical Sciences at NYU Shanghai, 3663 Zhongshan Road North, Shanghai 200062, China; and Santa Fe Institute, 1399 Hyde Park Road, Santa Fe, New Mexico 87501, USA



(Received 13 March 2020; accepted 30 April 2020; published 20 May 2020)

We study noise-induced creation and annihilation of magnetic droplet solitons in experimental parameter regions in which they are linearly stable against drift. Exploiting the rotational symmetry of the problem, we transform to the reference frame rotating with the droplet soliton and introduce an effective potential energy that accounts for the work done against spin transfer torque to rotate the magnetization between two different orientations. We use this function to compute the activation barrier in both directions between the uniform magnetization state and the droplet soliton state for a variety of nanocontact radii and currents. We investigate droplet soliton structures with both zero and nonzero spin-torque asymmetry parameters. Our approach can be applied to estimate activation barriers for dynamical systems where nongradient terms can be absorbed by changes of reference frames, and suggests a technique applicable to extended systems that may not be uniformly magnetized.

DOI: [10.1103/PhysRevB.101.184421](https://doi.org/10.1103/PhysRevB.101.184421)

I. INTRODUCTION

Magnetic droplet solitons are localized, dynamical magnetic textures that preserve their shape on timescales long compared to typical magnon relaxation times [1]. They are typically generated in spin-torque oscillators (STOs) [2] with a free layer and having perpendicular magnetic anisotropy [3], or in nanoconstrictions using pure spin currents generated by the spin Hall effect [4]. Unlike certain other textures, such as dynamical skyrmions [5], droplet solitons are not topologically protected and are sustained in driven systems via a balance between the competing effects of ordinary dissipation and an energy input provided by an external current acting through spin transfer torque (STT). Droplet solitons, dynamical skyrmions [5], and related textures, both topological and nontopological, have attracted substantial interest due both to their fundamental physical interest and also from the possibility of their applications in information storage, transfer, and manipulation.

Droplet solitons were first predicted by Ivanov and Kosevich [6] as “magnon droplets” in thin films formed by condensation of spin waves into a circular, uniformly precessing structure whose magnetization at the center points in the (nearly) opposite direction to that of the spins far away. In this formulation the deviation of the magnetization from the “up” direction (i.e., perpendicular to the plane) at infinity is proportional to the number of quantized spin waves excited. Ivanov and Kosevich restricted their analysis to conservative systems, i.e., no dissipation or spin torque; the resulting droplet structures were argued to be dynamically stable [7]. However, once dissipation—unavoidable in any

real system—is added, these structures quickly decay. For a review, see Kosevich *et al.* [1].

After the first experimental evidence [8] and direct observation [9] of droplet solitons, multiple experiments have generated and studied magnetic droplet solitons and related structures over the past several years [10–21]. The usual experimental situation leading to droplet soliton generation and decay occurs in a nanocontact spin-torque oscillator (NC-STO), where two magnetic layers are separated by a nonmagnetic spacer; the top layer is known as the free layer and the bottom layer as the fixed (or polarizing) layer. To generate droplet solitons, a nanocontact (typically with radius of order 100 nm, although it can vary) through which a current can be sent is placed on the free layer. This type of setup generates a spin transfer torque [22,23] to balance the effects of dissipation within the nanocontact region, thereby stabilizing the droplet soliton. An external magnetic field, usually perpendicular to the layers, is also applied, leading to the usual Larmor precession of spins and additional stabilizing effects [24].

Hofer, Silva, and Keller [25] were the first to show theoretically that magnetic droplet solitons can be formed in such nanocontacts. Using both analytical and numerical micromagnetic techniques, they studied droplet soliton shape profiles, small perturbations of the droplet soliton, nucleation processes, and related properties. One of their important conclusions was that the externally applied sustaining current singled out a specific droplet soliton precession frequency.

In a subsequent paper, Wills, Iacocca, and Hofer [26] (see also [27]) found that droplet solitons are linearly unstable at large bias currents, being subject to a drift instability in which

the droplet soliton center drifts outside of the nanocontact region. (This had been noticed a year earlier in micromagnetic simulations by Lendinez *et al.* [28]). Outside this region, dissipation is uncompensated because of the absence of STT, and the droplet soliton quickly decays. However, they also found that the droplet soliton *is* linearly stable in a narrow but experimentally accessible region of parameter space; see Fig. 2 of [26]. This figure shows three regions in the external field/applied current phase diagram for two nanocontact radii; the central region is where the droplet soliton is both sustained by the applied current and is linearly stable against drift.

This raises the question of lifetimes of linearly stable droplet solitons in this central region at low temperature: for a droplet soliton in this part of parameter space and centered in the nanocontact region, what are the extreme value statistics of a rare but large thermal (or other) fluctuation spontaneously arising and destroying the droplet soliton? This is important both for experimental studies of droplet solitons and possible future device applications, and this is the question we address in this paper.

In recent work, Moore and Hofer [27] computed decay of magnetic droplet solitons in the linearly stable region through a different mechanism, namely *thermally activated* ejection of the intact droplet soliton from the nanocontact region. In the region of parameter space in which the droplet soliton is linearly stable against drift, the decay mechanism studied here competes with the ejection mechanism, and which one dominates droplet soliton decay will depend on the experimental parameters. We will return to this question in the Discussion section.

The standard framework for analyzing activation over an energy (or more generally, action) barrier is provided by Kramers' theory [29] in which the transition rate τ^{-1} between two states separated by an energy barrier U follows to leading order an Arrhenius law $\tau^{-1} \sim \exp[-U/k_B T]$ when $k_B T \ll U$. In driven or otherwise nonequilibrium systems, such a barrier may be more difficult to properly define. In these cases, it is useful to employ a general path-integral approach to large deviations due to Wentzell and Freidlin [30], which rests on finding the most probable path in state space between two locally stable configurations. This approach is especially useful in dealing with nonequilibrium situations [31,32] and has been applied to thermally induced magnetic reversal under a variety of circumstances [33–37]. We will also utilize this approach in this paper.

The strategy employed in this paper consists of exploiting the rotational symmetries in the problem so that Kramers' theory of reversal rates can be applied in the presence of spin transfer torques. This is done in two steps. First, we introduce a pseudopotential [38] to account for the energy required to reorient the magnetization along a specific direction against the spin torque. The functional derivative of this term introduces an additional field, leading to an extra term in the Landau-Lifshitz-Gilbert equation that can be canceled by including an extra term with nonzero curl. In this way a new dynamic equation is obtained that is phenomenologically equivalent to the Landau-Lifshitz equation.

The second step requires transforming to a rotating frame where the polar axis is oriented along the fixed-layer polarization. In this new frame the nonzero-curl term vanishes and

the resulting simplified Landau-Lifshitz-Gilbert equation can be studied using Kramers' theory. We can then show that some important features are satisfied: in the rotating frame the effective energy decreases over time, and most importantly, the new set of equations leads to an equilibrium distribution for the Fokker-Planck equation. Satisfying these two requirements provides physical justification for the activation barriers calculated here.

The plan of the paper is as follows. In Secs. II–IV we describe the setup of the problem, introduce the magnetization dynamics, and discuss key aspects of the theory of conservative droplet solitons. We then describe in Sec. V the effects of spin transfer torque: we introduce the spin-torque pseudopotential, transform to a rotating reference frame, investigate the time evolution of the energy in this frame, and find the magnetization configurations corresponding to energy minima and saddle states. In Sec. VI we describe in detail the profiles of stationary configurations used to measure activation barriers. In Sec. VII, we examine the dynamical evolution of overdamped droplet solitons and find the droplet soliton profiles that are saddles, constituting transition states for droplet soliton creation and annihilation. The consequences of spatial dependence of the rate of rotation of the droplet soliton are discussed in Sec. VIII, where we show that the transition states can still be found for a nonzero spin-torque asymmetry parameter. In Sec. IX we calculate the Freidlin-Wentzell action for a chosen fluctuational trajectory that is traced in the class of shape-preserving precessional configurations and show that the action along that specific path equals double the pseudopotential energy introduced here, as would occur if the deterministic component of the dynamics were a simple gradient flow. Finally, in Sec. X we summarize our results, discuss the regions of parameter space where the theory breaks down, and briefly consider extensions of the theory and future work.

For completeness, the appendices provide additional derivations of many of the results used in the paper. Some of these can be found elsewhere in the literature, but they have been rederived here using notation consistent with the main text of this paper.

II. SETUP OF THE PROBLEM

We will study the situation of a spin-torque oscillator, as described in the Introduction, in which the free layer is a thin circular slab of radius ρ_{\max} and thickness d , with $d \ll \rho_{\max}$, and the uniform fixed-layer magnetization is given by $\mathbf{m}_f = (\sin \theta_f, 0, \cos \theta_f)$.

In the absence of currents and the resulting spin torques, the magnetization dynamics is described by the Landau-Lifshitz-Gilbert equation which can be presented in the following form. We introduce the linear operator \mathbb{L} acting on normalized fields and torques,

$$\mathbb{L} \equiv -\gamma' M_s [\mathbf{m} \times + \alpha \mathbf{m} \times \mathbf{m} \times], \quad (1)$$

where \mathbf{m} is the unit magnetization vector ($\mathbf{m} = \mathbf{M}/M_s$) in the free layer, M_s is the saturation magnetization, α is the damping coefficient, $\gamma' = \frac{\gamma_0}{1+\alpha^2}$ and $\gamma_0 = 2.211 \times 10^5 \frac{\text{m}}{\text{A}\cdot\text{s}}$ [39]. We hereafter confine ourselves to the constraint $|\mathbf{m}| \equiv 1$.

In this context, a ‘‘field’’ is understood as a variational derivative of an energy density \mathcal{E} and is normalized by M_s (i.e., $\mathbf{h}_{\text{eff}} = -\frac{1}{\mu_0 M_s^2} \frac{\delta \mathcal{E}}{\delta \mathbf{m}}$ for large samples, or $\mathbf{h}_{\text{eff}} = -\frac{\nabla_{\mathbf{m}} \mathcal{E}}{\mu_0 M_s^2}$ for a macrospin), and a ‘‘torque’’ is any term that contributes to the time rate of change of magnetic moment per unit volume. The effective field \mathbf{h}_{eff} is derived in Appendix A [cf. Eq. (A9)] and is separately given by [25]

$$\mathbf{h}_{\text{eff}} = \nabla^2 \mathbf{m} + \mathbf{h}_Z + \mathbf{h}_{\text{oe}} + (Q - 1)(\mathbf{m} \cdot \mathbf{n}_{\perp}) \mathbf{n}_{\perp}. \quad (2)$$

The first term on the right-hand side (RHS) of (2) corresponds to the exchange energy, \mathcal{E}_{ex} , associated with spatially varying magnetization; the second term is an externally applied static field \mathbf{h}_Z associated with the Zeeman energy $\mathcal{E}_Z = -\mathbf{m} \cdot \mathbf{h}_Z$; the third term corresponds to the Oersted field induced by a current (if present); and the final term is derived from the perpendicular magnetic anisotropy energy \mathcal{E}_K , consisting of two parts: $\mathbf{Q} = Q\mathbf{n}_{\perp}$ is the dimensionless crystalline anisotropy field (with $Q > 1$; cf. Appendix A), and $-(\mathbf{m} \cdot \mathbf{n}_{\perp})\mathbf{n}_{\perp}$ is the shape anisotropy (equivalently, demagnetizing field) for a thin film. In this equation all fields are normalized by the saturation magnetization magnitude M_s and space is normalized by the exchange length $l_{\text{ex}} = \sqrt{2A/\mu_0 M_s^2}$, where A is the exchange constant and μ_0 is the permeability of free space. The geometry of the setup appears in Fig. 1.

Using this operator the zero-temperature magnetization dynamics can be written in the compact form [40,41]

$$\dot{\mathbf{m}} = \mathbb{L} \mathbf{h}_{\text{eff}}. \quad (3)$$

To account for thermal effects in a region of volume $dV = l_{\text{ex}}^2 d$ an additional noise term $\sqrt{2\eta} \dot{\mathbf{W}}$ can be added to the effective field [40,41]. Here, $\dot{\mathbf{W}}$ is a three-dimensional normally distributed stochastic white noise process and the noise strength η is given by $\eta = \frac{\alpha k_B T}{2Ad\gamma_0 M_s}$.

If the system above is now driven by an STT-inducing current I with contact radius ρ^* , an additional nonconservative term must be added to (3). This results in the Landau-Lifshitz-Gilbert-Slonczewski (LLGS) equation [42]

$$\dot{\mathbf{m}} = \mathbb{L} \mathbf{h}_{\text{eff}} - \frac{\sigma \gamma_0 M_s V(\mathbf{r})}{1 + \alpha^2} \left[\frac{\alpha \mathbf{m} \times \hat{\mathbf{m}}_p - \mathbf{m} \times \mathbf{m} \times \hat{\mathbf{m}}_p}{1 + \nu \mathbf{m} \cdot \hat{\mathbf{m}}_p} \right], \quad (4)$$

where $\hat{\mathbf{m}}_p$ is the magnetization direction of the fixed layer, ν is the spin-torque asymmetry parameter (with $0 \leq \nu < 1$), $V(\mathbf{r})$ describes the spatial distribution of the (cylindrically symmetric) current, and $\sigma = J/J_0$, with $J_0 = \frac{\mu_0 e d M_s^2}{\hbar}$ the magnitude of the reduced current density [25,26]. Equation (4) is the starting point of the analysis in this paper.

III. MAGNETIZATION EQUATIONS OF MOTION

Following [25], we begin by studying the high-symmetry case where the free layer lies in the xy plane, $\mathbf{h}_{\text{oe}} = 0$ and $\mathbf{h}_Z = h_Z \hat{\mathbf{z}}_L$. (This and the following section are mostly a review of the procedures followed and results obtained in [25]).

Given that $|m| = 1$, it is useful to parametrize \mathbf{m} in terms of fixed spherical coordinates

$$\mathbf{m} = (\cos \Phi \sin \Theta, \sin \Phi \sin \Theta, \cos \Theta) \quad (5)$$

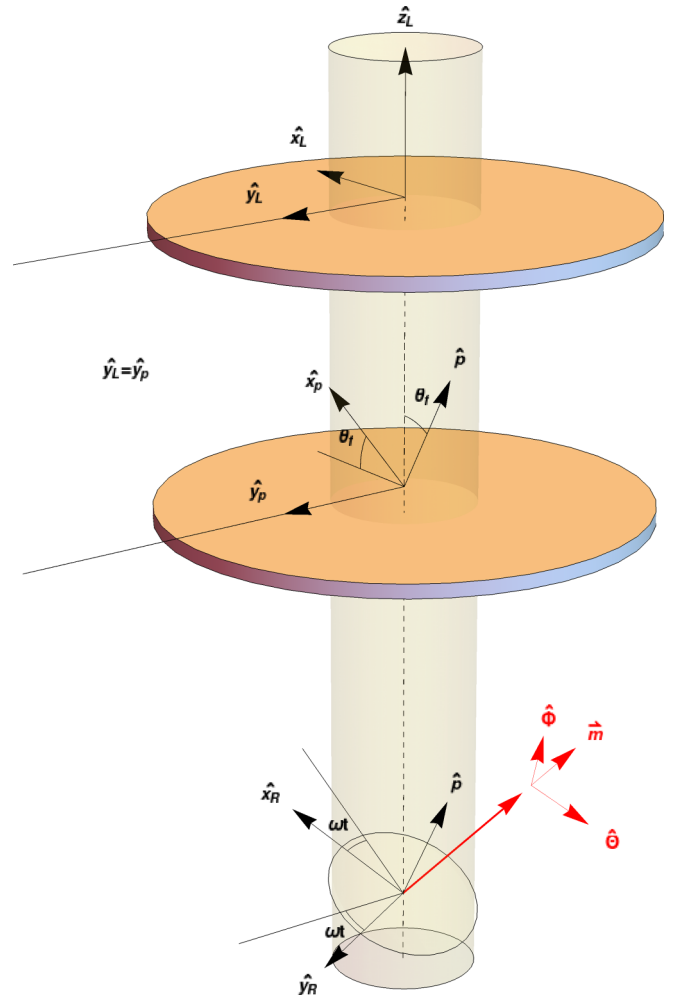


FIG. 1. Geometry of setup and coordinate systems. Current flows upward from layer. The three coordinate systems of relevance are (I) the laboratory frame $\{\hat{\mathbf{x}}_L, \hat{\mathbf{y}}_L, \hat{\mathbf{z}}_L\}$ where $\hat{\mathbf{z}}_L = \mathbf{n}_{\perp}$ is the normal to the film plane, (II) the fixed-layer frame $\{\hat{\mathbf{x}}_P, \hat{\mathbf{y}}_P, \hat{\mathbf{m}}_P\}$ where the polarization vector $\hat{\mathbf{m}}_P$ makes an angle θ_f with \mathbf{n} , and (III) the rotating frame $\{\hat{\mathbf{x}}_R, \hat{\mathbf{y}}_R, \hat{\mathbf{m}}_P\}$, which rotates about $\hat{\mathbf{m}}_P$ with frequency ω . Additionally, the set of eigenvectors of the operator $\mathbb{L}^T \mathbb{L}$ are shown in red; these correspond to the set $\{\mathbf{m}, \hat{\Theta}, \hat{\Phi}\}$.

and to write the field as $\mathbf{h}_{\text{tot}} = h_{\Phi} \hat{\Phi} + h_{\Theta} \hat{\Theta} + h_m \mathbf{m}$, where the unit vectors are shown in Fig. 1.

Inserting (5) into the LLGS equation (4) yields partial differential equations (PDEs) for Θ and Φ , which are given in [25] for $\alpha \rightarrow 0$. Because they will be used below, we reproduce them here for arbitrary α (for easy comparison, we use the same notation as [25]):

$$\frac{\dot{\Theta}}{\gamma' M_s} = F - \alpha \left(G - \frac{\sigma}{\alpha} V P_{\Theta} \right) + \alpha \sigma V P_{\Phi} \quad (6)$$

and

$$\sin \Theta \frac{\dot{\Phi}}{\gamma' M_s} = G + \alpha \left(F + \frac{\sigma}{\alpha} V P_{\Phi} \right) + \alpha \sigma V P_{\Theta}, \quad (7)$$

where $V = V(\rho)$ and F, G, P_Φ , and P_Θ are functions of Φ and Θ and are given by

$$F[\Theta, \Phi] = \sin \Theta \nabla^2 \Phi + 2 \cos \Theta \nabla \Phi \cdot \nabla \Theta, \quad (8)$$

$$G[\Theta, \Phi] = -\nabla^2 \Theta + \frac{1}{2} \sin(2\Theta)(|\nabla \Phi|^2 + Q - 1) + h_Z \sin \Theta, \quad (9)$$

$$P_\Theta(\Theta, \Phi) = \frac{-\cos \Theta \cos \Phi \sin \theta_f + \sin \Theta \cos \theta_f}{1 + \nu(\cos \Phi \sin \Theta \sin \theta_f + \cos \Theta \cos \theta_f)}, \quad (10)$$

$$P_\Phi(\Theta, \Phi) = \frac{\sin \Phi \sin \theta_f}{1 + \nu(\cos \Phi \sin \Theta \sin \theta_f + \cos \Theta \cos \theta_f)}. \quad (11)$$

Following Hofer *et al.* [25], we rescale length, time, current, and field parameter to remove the explicit dependence on γ' and Q (recall $Q > 1$):

$$\rho = \rho' / \sqrt{Q - 1}, \quad \gamma' M_s t = t' / (Q - 1), \quad (12)$$

$$\sigma = (Q - 1)\sigma', \quad h_Z = (Q - 1)h'_Z, \quad \rho_{\max} = \rho'_{\max} / \sqrt{Q - 1}.$$

Finally, our boundary conditions stipulate that

$$\Theta(\rho', \phi, t') = 0 \text{ at } \rho' = \rho'_{\max}; \quad \frac{\partial \Theta}{\partial \rho'} = 0 \text{ at } \rho' = 0. \quad (13)$$

That is, the magnetization is uniformly in the $+\hat{z}_L$ direction outside the nanocontact. (Our boundary condition differs from that of [25] only in that the latter takes $\rho'_{\max} \rightarrow \infty$). The boundary condition at $\rho' = 0$ ensures regularity of solutions. A general treatment of boundary conditions is given in Appendix A.

IV. CONSERVATIVE DROPLET SOLITON PROFILES

We consider first the case of a conservative system, i.e., $\alpha = \sigma' = 0$. The droplet soliton solution in this case is given by Hofer *et al.* [25]; we briefly review it here. Although this situation is unphysical, the solution serves as a starting point for consideration of realistic situations.

The simplest (and most relevant) solution is one where the magnetization precesses uniformly, i.e., $\Phi(\rho', \phi, t') = \Phi(t')$. In this case, Eq. (8) gives $F[\theta, \Phi] = 0$, and consequently Eq. (6) indicates that Θ is independent of time. Introducing ω_0 as a precessional frequency parameter, we can write

$$\Phi(t') = (\omega_0 + h'_Z)t', \quad (14)$$

which, using Eq. (7), results in a differential equation for $\Theta = \Theta_0(\rho'; \omega_0)$:

$$\left(\frac{d^2}{d\rho'^2} + \frac{1}{\rho'} \frac{d}{d\rho'} \right) \Theta_0 - \frac{1}{2} \sin(2\Theta_0) + \omega_0 \sin \Theta_0 = 0. \quad (15)$$

This equation plus the boundary conditions (13) determine the conservative droplet soliton profile $\Theta(\rho'; \omega_0)$.

Before proceeding, we note two features of these equations. First, because $0 < \omega_0 < 1$ [25], the droplet soliton

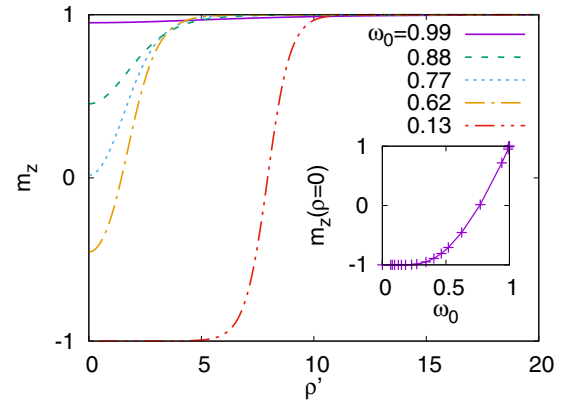


FIG. 2. Conservative droplet soliton profiles for different ω_0 . The amplitude of each droplet soliton at the origin $m_z(\rho = 0)$ is given next to the frequency. The inset shows the values of the amplitude of the droplet soliton for different shape parameters ω_0 .

precession frequency $\omega_0 + h'_Z$ varies between the Zeeman frequency h'_Z and the FMR frequency $1 + h'_Z$. This fact plus Eqs. (13) and (15) shows that $m_z(\rho' = 0; \omega_0) > -1$ independently of ω_0 .

Second, the frequency ω_0 appears as a free parameter in the solution; it can take any value between 0 and 1 in a conservative system (if it existed). This is an important difference with realistic situations in which STT counterbalances dissipation; there the droplet soliton precessional frequency is determined by the strength of the applied current [25]. We return to nonconservative systems later. For now, we simply note that droplet soliton profiles $\Theta(\rho'; \omega_0)$ are parametrized by ω_0 .

Equation (15) must be solved using numerical means [43]. Figure 2 shows several solutions for different ω_0 (conservative droplet soliton profiles are also given in Fig. 2 of [25]).

We remark on several features of the conservative droplet soliton profiles shown in Fig. 2. We note first that $m_z(0; \omega_0)$ is a monotonically increasing function of ω_0 ; in particular, $m_z(0; \omega_0) \rightarrow -1$ as $\omega_0 \rightarrow 0$ and $m_z(0; \omega_0) \rightarrow +1$ as $\omega_0 \rightarrow 1$. (The latter is unsurprising; as $\omega_0 \rightarrow 1$ the droplet soliton becomes the uniform state precessing at the FMR frequency.) We also note that, except for ω_0 close to 1, the region in which Θ_0 varies significantly with ρ' is relatively narrow.

Even though these soliton droplet profiles correspond to an unphysical situation (i.e., absence of dissipation), they will become important in the subsequent discussion where $\sigma \neq 0$ and $\alpha \neq 0$. In particular we will be focusing on solutions of Eqs. (6) and (7) that preserve shape (i.e., $\dot{\Theta} = 0$) and have uniform precessional frequency ($\frac{d\Phi}{dt'} = \omega$). It can be easily verified that for the highly symmetric case $P_\Phi = 0$, these are equivalent conditions: $(1 + \alpha^2)G[\Theta, \Phi] = \omega \sin \Theta$ and $F[\Theta, \Phi] = \alpha G[\Theta, \Phi] - \sigma V P_\Theta$.

V. EFFECTS OF SPIN TRANSFER TORQUE

In order to account for the effects of spin transfer torque, we introduce a term in the action corresponding to an energy

density of a pseudopotential:

$$\mathcal{E}_{\text{ST}} = \begin{cases} \mu_0 M_s^2 \frac{\sigma V(\rho)}{\alpha} \mathbf{m} \cdot \hat{\mathbf{m}}_p, & \nu = 0, \\ \mu_0 M_s^2 \frac{\sigma V(\rho)}{\alpha} \frac{\ln[1 + \nu \mathbf{m} \cdot \hat{\mathbf{m}}_p]}{\nu}, & \nu \neq 0. \end{cases} \quad (16)$$

This can be used to derive an effective field on the system arising from the spin torque:

$$\mathbf{h}_{\text{ST}} = -\frac{1}{\mu_0 M_s^2} \frac{\delta \mathcal{E}_{\text{ST}}}{\delta \mathbf{m}} = -\frac{\sigma V(\rho)}{\alpha} \frac{\hat{\mathbf{m}}_p}{1 + \nu \mathbf{m} \cdot \hat{\mathbf{m}}_p}. \quad (17)$$

The total field is now given by $\mathbf{h}_{\text{tot}} = \mathbf{h}_{\text{eff}} + \mathbf{h}_{\text{th}} + \mathbf{h}_{\text{ST}}$, and the equations for magnetization dynamics, now including spin polarized currents and thermal fluctuations, become

$$\dot{\mathbf{m}} = \mathbb{L} \mathbf{h}_{\text{tot}} - \gamma_0 M_s \frac{\sigma V(\rho)}{\alpha} \left[\frac{\mathbf{m} \times \hat{\mathbf{m}}_p}{1 + \nu \mathbf{m} \cdot \hat{\mathbf{m}}_p} \right] \quad (18)$$

$$= \mathbb{L} \mathbf{h}_{\text{tot}} - \frac{\gamma_0}{\mu_0 M_s} \nabla_{\mathbf{m}} \times (\mathbf{m} \mathcal{E}_{\text{ST}}). \quad (19)$$

Equation (18) is a compact version of the stochastic Landau-Lifshitz-Gilbert-Slonczewski equation, and will be our starting point for further analysis. We note in particular that the curl term is inversely proportional to α , and so becomes important for small α . Notice that, in contrast with the factor of γ' used in the definition of \mathbb{L} , the curl term uses γ_0 instead.

With the addition of \mathcal{E}_{ST} , the pseudoenergy becomes $\mathcal{E}_{\text{tot}} = \mathcal{E}_{\text{ex}} + \mathcal{E}_K + \mathcal{E}_Z + \mathcal{E}_{\text{ST}}$, where the terms correspond, respectively, to exchange, effective anisotropy, Zeeman, and spin-torque pseudopotential. When convenient, we will use the reduced version of these energies $\mathcal{E}' = \frac{\mathcal{E}}{\mu_0 M_s^2}$.

A. Transformation to a rotating reference frame

The spin-torque term on the RHS of (19) cannot be algebraically manipulated into a form that is the gradient of a smooth potential. However, in the limit of low asymmetry parameter $\nu \rightarrow 0$ and uniform current density, it provides useful information on how the time derivatives of the various vectors transform between a fixed reference frame and a rotating reference frame. We now provide this expression explicitly.

Consider a reference frame uniformly rotating with frequency ω about a fixed axis $\hat{\Omega}$. The transformation of the time derivatives of a vector \mathbf{u} between the fixed and the rotating frames is given by

$$\dot{\mathbf{u}} = \dot{\mathbf{u}} + \omega \hat{\Omega} \times \mathbf{u}, \quad (20)$$

where $\dot{\mathbf{u}}$ and $\dot{\mathbf{u}}$ denote the vector in the fixed and rotating frames, respectively.

Equation (18) describes the dynamics of the magnetization in a fixed reference frame. It will be useful to transform to a reference frame that rotates about $\hat{\mathbf{m}}_p$ with frequency $\omega_{\text{ST}} = \frac{\sigma \gamma_0 M_s V(\rho)}{\alpha}$. In this frame the magnetization evolves as

$$\dot{\mathbf{m}}_{\text{rotating frame}} = \mathbb{L} \tilde{\mathbf{h}}_{\text{tot}}. \quad (21)$$

If the energy functional is rotationally symmetric with respect to $\hat{\mathbf{m}}_p$, the fields in the rotating frame are time independent, and (21) describes an autonomous dynamical system. The approach of Serpico *et al.* [44] can be used to

show that the magnetization in this frame evolves toward the nearest energy minimum. It will further become evident that in the rotating frame the magnetization of a macrospin reaches thermal equilibrium even when $\nu \neq 0$.

To analyze droplet soliton behavior in the presence of STT, we insert (5) into the LLGS equation (18) and rescale with (12) to obtain equations for Θ and Φ :

$$\dot{\Theta} = h_{\Phi} + \alpha h_{\Theta} - \frac{\sigma' V(\rho')}{\alpha'} P_{\Phi} \quad (22)$$

and

$$\sin \Theta \dot{\Phi} = -h_{\Theta} + \alpha h_{\Phi} + \frac{\sigma' V(\rho')}{\alpha'} P_{\Theta}, \quad (23)$$

where $P_{\Phi} = -\frac{\hat{\mathbf{m}}_p \cdot \hat{\Phi}}{1 + \nu \mathbf{m} \cdot \hat{\mathbf{m}}_p}$, $P_{\Theta} = -\frac{\hat{\mathbf{m}}_p \cdot \hat{\Theta}}{1 + \nu \mathbf{m} \cdot \hat{\mathbf{m}}_p}$, $h_{\Phi} = \mathbf{h}_{\text{tot}} \cdot \hat{\Phi}$, $h_{\Theta} = \mathbf{h}_{\text{tot}} \cdot \hat{\Theta}$, and $\alpha' = \frac{\alpha}{1 + \alpha^2}$.

Each component of the field can be separated into terms corresponding to each type of energy density (e.g., $h_{\Theta} = h_{\text{ex},\Theta} + h_{Z,\Theta} + h_{K,\Theta} + h_{\text{ST},\Theta}$). We provide explicit expressions for all field terms in Appendix E.

As they are written above, the time evolution equations (22) and (23) are valid for any fixed coordinate system regardless of the direction of the polar axis. If $\hat{\mathbf{m}}_p$ is chosen as the polar axis, the last term in (22) vanishes, and P_{Θ} becomes independent of Φ . Furthermore, when passing to a reference frame rotating about $\hat{\mathbf{m}}_p$ with frequency $\frac{\sigma'}{\alpha'}$, an additional term $\frac{\sigma'}{\alpha'} \sin \Theta$ must be subtracted from (23). In that frame $\Theta = \tilde{\Theta}$. Dropping the explicit references to the dependencies on Θ and Φ we have, in the rotating frame,

$$\dot{\Theta} = h_{\Phi} + \alpha h_{\Theta} \quad (24)$$

and

$$\sin \Theta \dot{\Phi} = -h_{\Theta} + \alpha h_{\Phi} + \frac{\sigma'}{\alpha'} [V P_{\Theta} - \sin \Theta]. \quad (25)$$

The bracket vanishes when $\nu = 0$ and the current strength is uniform in the region occupied by the droplet soliton.

Equations (22) and (23) for the static reference frame are closely related to those given in [25] [Eqs. (3) and (4) of that paper], where $\hat{\mathbf{m}}_p$ and \mathbf{h} both point perpendicularly to the plane. In that specific case the following relations hold:

$$F[\Theta, \Phi] = h_{\Phi} - \frac{\sigma' V(\rho')}{\alpha} P_{\Phi} \quad (26)$$

and

$$G[\Theta, \Phi] = \frac{\sigma' V(\rho')}{\alpha} P_{\Theta} - h_{\Theta}. \quad (27)$$

For magnetization configurations where the azimuthal angle is not uniform, the exchange interaction introduces complications that will be examined perturbatively for small ν (Sec. VIII). To understand the origin of these complications, we use [cf. Eq. (5)] spherical coordinates for the magnetization \mathbf{m} , where now Θ is the polar angle that \mathbf{m} makes with $\hat{\mathbf{m}}_p$ and Φ is the azimuthal angle in the plane perpendicular to $\hat{\mathbf{m}}_p$. The rotational symmetry requirement indicates that for constant Φ the azimuthal component of the exchange field is zero (i.e., $h_{\text{ex},\Phi} = -\frac{1}{\sin \Theta} \frac{\delta \mathcal{E}_{\text{ex}}}{\delta \Phi} = 0$). However, in a nonuniform configuration this no longer need be the case: the azimuthal field depends on the spatial profile of Φ .

Using the scaling Eq. (12) the exchange-induced azimuthal field is given by

$$h_{\text{ex},\Phi} = -\frac{1}{\sin\Theta} \left[\frac{\partial \mathcal{E}_{\text{ex}}}{\partial \Phi} - \nabla \left(\frac{\partial \mathcal{E}_{\text{ex}}}{\partial \nabla \Phi} \right) \right] \quad (28)$$

$$= [\nabla^2 \Phi \sin\Theta + \nabla \Phi \cdot \nabla \Theta \cos\Theta]. \quad (29)$$

Because this expression is generally nonzero, the energy will change as the magnetization rotates about $\hat{\mathbf{m}}_p$. The case of constant Φ is not valid when $\nu \neq 0$ or $\rho^* \neq \infty$, as it changes with a Θ -dependent rate obtained from the second term in Eq. (18):

$$-\omega_{\text{ST}} \left[\frac{\mathbf{m} \times \hat{\mathbf{m}}_p}{1 + \nu \mathbf{m} \cdot \hat{\mathbf{m}}_p} \right] \cdot \left[\frac{\hat{\Phi}}{\sin\Theta} \right] = \frac{\omega_{\text{ST}}}{1 + \nu \cos\Theta}. \quad (30)$$

This would imply that in an extended magnet the value of Φ will lag in some regions compared to others. In general, the curl term in (19) will not be absorbed into a common rotating frame for the full magnet and, unless certain conditions are satisfied [45–47], the Gibbs distribution is no longer a stationary solution of the Fokker-Planck equation for the micromagnetic system.

In Appendix D, we discuss the Θ dependence of this precessional rate in the case of uniaxial macrospins. The rest of this paper is concerned with shape-preserving precessional states which may have, in addition to ω_{ST} , additional frequency shifts $\omega^{(1)}$ which must have the same value in any reference frame.

A quantity that will appear repeatedly in the subsequent discussion is

$$\Xi \equiv \mathbf{m} \cdot \left(\frac{\delta \mathcal{E}'_{\text{tot}}}{\delta \mathbf{m}} \times \nabla_{\mathbf{m}} \mathcal{E}'_{\text{ST}} \right), \quad (31)$$

which measures the degree of misalignment between fields obtained from the total energy functional \mathcal{E}_{tot} and from the spin-torque pseudopotential \mathcal{E}_{ST} . More generally, it is a measure of the time rate of energy change for a magnetization configuration that appears stationary in the rotating frame. We highlight the fact that for the rotationally symmetric systems discussed here this reduces to

$$\Xi \equiv h_{\text{ex},\Phi} h_{\text{ST},\Theta}, \quad (32)$$

and becomes zero if $h_{\text{ex},\Phi} = 0$.

B. Magnetization dynamics in the rotating frame

Moving to the rotating frame when $\nu = 0$ has the advantage that configurations which are critical points of the energy landscape ($h_{\Theta} = h_{\Phi} = 0$) also become stationary dynamical points ($\dot{\Theta} = \dot{\Phi} = 0$). This allows us to identify the saddle states through which the magnetization passes in switching from the basin of attraction of one local energy minimum to that of another. In this section we examine the effects on the various relevant physical quantities of moving to the rotating frame.

To proceed it is useful to define a set of Euler rotations. We start by selecting $\hat{\mathbf{y}} = \hat{\mathbf{p}} \times \hat{\mathbf{z}}_L$ as the axis of nodes, and define $\hat{\mathbf{x}}$ to complete a right-handed set of coordinates: $\hat{\mathbf{x}} = \hat{\mathbf{y}} \times \hat{\mathbf{z}}$.

Transformation of vectors from the laboratory frame to the stationary frame aligned with $\hat{\mathbf{m}}_p$ can be effected using the rotation matrix

$$\mathcal{R}_{P \leftarrow L} = \begin{pmatrix} \cos\theta_f & 0 & \sin\theta_f \\ 0 & 1 & 0 \\ -\sin\theta_f & 0 & \cos\theta_f \end{pmatrix}. \quad (33)$$

Similarly, transforming from the polarized frame to the rotating frame can be done using the matrix

$$\mathcal{R}_{R \leftarrow P} = \begin{pmatrix} \cos\omega t & \sin\omega t & 0 \\ -\sin\omega t & \cos\omega t & 0 \\ 0 & 0 & 1 \end{pmatrix}. \quad (34)$$

The combined transformation matrix, from the laboratory frame to the rotating frame, is therefore

$$\begin{aligned} \mathcal{R}_{\omega t} &= \mathcal{R}_{R \leftarrow P} \mathcal{R}_{P \leftarrow L} \\ &= \begin{pmatrix} \cos\omega t \cos\theta_f & \sin\omega t & \cos\omega t \sin\theta_f \\ -\sin\omega t \cos\theta_f & \cos\omega t & -\sin\omega t \sin\theta_f \\ -\sin\theta_f & 0 & \cos\theta_f \end{pmatrix}. \end{aligned} \quad (35)$$

Notice that in this convention the angle θ_f is measured from $\hat{\mathbf{m}}_p$ to $\hat{\mathbf{z}}_L$. The reader is reminded that, because the transformation is unitary, the inverse matrix $\mathcal{R}_{\omega t}^{-1}$ is simply the transpose $\mathcal{R}_{\omega t}^T$.

The exchange energy term $\nabla^2 \mathbf{m}$ is invariant under rotation of the coordinate system. For the remaining terms in the energy, the corresponding fields transform and become time dependent:

$$\mathbf{h}_{\text{rotating frame}} = \mathcal{R}_{\omega t} \mathbf{h}_{\text{lab frame}}. \quad (36)$$

The Landau-Lifshitz operator \mathbb{L} transforms as well:

$$\mathbb{L}_{\text{rotating frame}} = \mathcal{R}_{\omega t} \mathbb{L}_{\text{lab frame}} \mathcal{R}_{\omega t}^{-1}. \quad (37)$$

Combining Eqs. (20) and (36) allows us to determine how the time derivatives of vectors transform on switching from the laboratory to the rotating frame:

$$\dot{\mathbf{u}}_{\text{rotating frame}} = \dot{\mathcal{R}}_{\omega t} \mathbf{u}_{\text{lab frame}} + \mathcal{R}_{\omega t} \dot{\mathbf{u}}_{\text{lab frame}}. \quad (38)$$

We choose $t = 0$ to be the time when the coordinate axes of the rotational frame coincide with the polarizer frame. Then $\mathcal{R}_{\omega t=0} = \mathcal{R}_{P \leftarrow L}$ and $\dot{\mathcal{R}}_{\omega t} = \dot{\mathcal{R}}_{R \leftarrow P, t=0} \mathcal{R}_{P \leftarrow L}$, and the time derivative matrix at $t = 0$ can be written succinctly as the cross product

$$\dot{\mathcal{R}}_{R \leftarrow P} = \omega \begin{pmatrix} 0 & 1 & 0 \\ -1 & 0 & 0 \\ 0 & 0 & 0 \end{pmatrix} = -\omega \hat{\mathbf{m}}_p \times. \quad (39)$$

Finally, the full transformation of time derivatives from the laboratory frame into the rotating frame is

$$\dot{\mathbf{u}}_{\text{rotating frame}} = -\omega \hat{\mathbf{m}}_p \times \mathcal{R}_{P \leftarrow L} \mathbf{u}_{\text{lab frame}} + \mathcal{R}_{P \leftarrow L} \dot{\mathbf{u}}_{\text{lab frame}}. \quad (40)$$

We next examine how vectors that are constant in the laboratory frame behave in the rotating frame. For small misalignments between $\hat{\mathbf{m}}_p$ and \mathbf{n} , $\mathcal{R}_{P \leftarrow L} \approx (\mathbf{1} + \theta_f \hat{\mathbf{y}} \times)$

and so

$$\dot{\mathbf{u}}_{\text{rotating frame}} = -\omega \hat{\mathbf{m}}_p \times \mathcal{R}_{P \leftarrow L} \mathbf{u}_{\text{lab frame}} \quad (41)$$

$$\approx -\omega \hat{\mathbf{m}}_p \times (\mathbf{1} + \theta_f \hat{\mathbf{y}}_L \times) \mathbf{u}_{\text{lab frame}}. \quad (42)$$

Fields that are constant in the laboratory frame will become time dependent in the rotating frame if the RHS of (41) is nonzero. However, the RHS does become zero in the symmetric scenario in which $\theta_f = 0$ and the external fields are aligned with $\hat{\mathbf{m}}_p$. (This is the case considered by Hofer *et al.* [25]).

We emphasize that the symmetry condition discussed above is somewhat more restrictive than simple cylindrical symmetry. The rotational symmetry must be satisfied point-by-point in the full sample; it is not sufficient that the full problem alone is invariant under a global rotation about a common axis. In particular, the Oersted field and the edge-anisotropy fields do not satisfy this more restrictive symmetry requirement. In the rotational frame centered at an arbitrary point away from the axis of the disk, both fields appear to be circularly polarized. As a result, this will introduce self-oscillations in the rotating frame that will be reflected as quasiperiodicities in the laboratory frame. The proper treatment of this quasiperiodic scenario is beyond the scope of this work; we restrict ourselves here to the study of reversal in the high-symmetry case. However, we anticipate that the concepts discussed below for cases in which $\theta_f \neq 0$ will be of importance for the proper treatment of the Oersted field.

The pseudoenergy defined in Appendix A is, after rescaling [Eq. (12)],

$$\mathcal{E}'_{\text{tot}} = |\nabla' \mathbf{m}|^2 - (\mathbf{m} \cdot \hat{\mathbf{z}}_L)^2 - \mathbf{m} \cdot \mathbf{h}'_0 + \mathcal{E}'_{\text{ST}}. \quad (43)$$

This quantity is a scalar and will therefore be invariant under rotational transformations. The first and last terms on the RHS are unaffected by changes in reference frame, but the second (magnetostatic) and third (Zeeman) terms are specified for fields that are constant in the laboratory frame. As we move to the rotating frame their energy densities become harmonically dependent on time. The rate of change of those quantities is given by

$$\frac{d}{dt} [(\mathbf{m} \cdot \hat{\mathbf{z}}_L)^2] = 2(\mathbf{m} \cdot \hat{\mathbf{z}}_L)[\dot{\mathbf{m}} \cdot \hat{\mathbf{z}}_L + \mathbf{m} \cdot \dot{\hat{\mathbf{z}}}_L] \quad (44)$$

and

$$\frac{d}{dt} [\mathbf{m} \cdot \mathbf{h}_0] = \dot{\mathbf{m}} \cdot \mathbf{h}_0 + \mathbf{m} \cdot \dot{\mathbf{h}}_0. \quad (45)$$

More generally, for anisotropy energies of polynomial type with respect to specific directions $\hat{\mathbf{u}}$, i.e., $\mathcal{E}'_K = \sum_n K_n (\mathbf{m} \cdot \hat{\mathbf{u}}_n)^n$, we can decompose the field $\mathbf{h} = \sum_n \mathbf{h}_n$ into terms $\mathbf{h}_n = -nK_n (\mathbf{m} \cdot \hat{\mathbf{u}}_n)^{n-1} \hat{\mathbf{u}}_n$ and rewrite the energy as $\mathcal{E}'_K = -\sum_n \frac{\mathbf{m} \cdot \mathbf{h}_n}{n}$ so that

$$\frac{d\mathcal{E}'_K}{dt} = \sum_n nK_n (\mathbf{m} \cdot \hat{\mathbf{u}}_n)^{n-1} [\hat{\mathbf{u}}_n \cdot \dot{\mathbf{m}} + \dot{\hat{\mathbf{u}}}_n \cdot \mathbf{m}] \quad (46)$$

$$= \mathbf{h} \cdot \dot{\mathbf{m}} + \sum_n nK_n (\mathbf{m} \cdot \hat{\mathbf{u}}_n)^{n-1} \dot{\hat{\mathbf{u}}}_n \cdot \mathbf{m}. \quad (47)$$

The scalar product is unaffected when switching to the moving frame. Since in the rotating frame $\dot{\mathbf{m}} = \mathbb{L} \mathbf{h}$, and $\dot{\hat{\mathbf{u}}}$ is given

by (41), we arrive finally at

$$\frac{d\mathcal{E}'}{dt} \approx -\alpha |\mathbf{h}_{\text{tot}}|^2 - \omega [\hat{\mathbf{m}}_p \times (\mathbf{1} + \theta_f \hat{\mathbf{y}}_L \times) \mathbf{h}_{\text{lab frame}}] \cdot \mathbf{m}. \quad (48)$$

It is convenient to keep in mind that $\hat{\mathbf{m}}_p \times \mathbf{h}_{\text{ST}} = 0$, so the cross product in the parentheses will require only the terms for \mathbf{h}_{eff} given in (2). In the symmetric case ($\theta_f = 0$) we find

$$\begin{aligned} \frac{d\mathcal{E}'_{\text{tot}}}{dt} &= -\alpha |\mathbf{h}_{\text{tot}}|^2 - \left(\omega \hat{\mathbf{m}}_p \times \frac{\delta \mathcal{E}'}{\delta \mathbf{m}_{\text{lab}}} \right) \cdot \mathbf{m} \\ &= -\alpha |\mathbf{h}_{\text{tot}}|^2 - \left(\nabla_{\mathbf{m}} \mathcal{E}'_{\text{ST}} \times \frac{\delta \mathcal{E}'}{\delta \mathbf{m}_{\text{lab}}} \right) \cdot \mathbf{m} \\ &= -\alpha |\mathbf{h}_{\text{tot}}|^2 + \Xi. \end{aligned} \quad (49)$$

From this we see that, in the absence of Ξ , the system will evolve toward lower energies. The term Ξ is zero when the fields are aligned with $\hat{\mathbf{m}}_p$; if not, then its magnitude oscillates as the system rotates about $\hat{\mathbf{m}}_p$. Self-oscillations occur if the total energy change is zero after a full periodic orbit:

$$\Delta \mathcal{E}' = (-\alpha |\mathbf{h}_{\text{tot}}|^2 + \Xi) dt = 0. \quad (50)$$

A similar quantity, known as the Melnikov function [42], quantifies the energy change as the magnetization performs one cycle in the conservative dynamics ($\alpha = 0$). The calculation of that quantity requires precise knowledge of the equal energy orbits and is the basis of calculations based on the method of averaging [48,49]. Equation (50) can be used from either the stationary or the rotating reference frames. At this point, the meaning of Ξ becomes apparent: it is a spin-torque-induced power density influx. For a given magnetization orientation energy is dissipated by damping at a rate $\alpha |\mathbf{h}_{\text{tot}}|^2$ while the spin-torque term injects energy into the system; the curl term in Eq. (19) is the cause of this power influx. Because it is perpendicular to \mathbf{h}_{ST} , the effective spin-torque energy cannot increase; rather, the energy will flow into the other energy terms (\mathcal{E}_{ex} , \mathcal{E}_K , or \mathcal{E}_Z).

Because the external fields considered here are aligned with $\hat{\mathbf{m}}_p$, they do not contribute to a change in the energy as the reference frame rotates. However, the same cannot be said for the exchange field since its direction depends on the instantaneous spatial distribution of the magnetization. Nevertheless, $\Xi = 0$ for the set of solutions of the equation $F[\Theta, \Phi] = 0$. If Φ is small, then contributions of its nonuniformities can be neglected when calculating $G[\Theta, \Phi]$.

Summarizing the above discussion: by moving to the rotating frame, it is possible to find stationary solutions if external fields are parallel to the fixed-layer polarization; if not, then the solutions display small self-oscillations. In the vicinity of these configurations, the energy is guaranteed to decrease at every cycle. We postulate (and will justify below) that these configurations either play the role of transition barriers or else are metastable configurations.

VI. STATIONARY SOLUTIONS IN THE ROTATING FRAME

We are now in a position to discuss the stationary solutions of Eqs. (24) and (25); as described above, we restrict ourselves to the case where Φ is spatially uniform, so that $h_\Phi = 0$. In

the rotating frame the bracket vanishes when $\nu = 0$ and as a consequence stationary solutions require that $h_\Theta = 0$ as well.

We will refer to this highly symmetric scenario in which $\theta_Z = \theta_f = \nu = 0$ as the unperturbed case, with solutions $\Phi_0 = 0$ and $\Theta_0(\mathbf{r})$. The equations then become

$$\begin{aligned} h_\Theta^{(0)} &= h_{\text{ex},\Theta}^{(0)} + h_{Z,\Theta}^{(0)} + h_{K,\Theta}^{(0)} + h_{\text{ST},\Theta}^{(0)}, \\ 0 &= \nabla'^2 \Theta_0 - h_Z \sin \Theta_0 - \frac{1}{2} \sin 2\Theta_0 + \frac{\sigma' V}{\alpha} \sin \Theta_0, \end{aligned} \quad (51)$$

and

$$h_\Phi^{(0)} = h_{\text{ex},\Phi}^{(0)} + h_{Z,\Phi}^{(0)} + h_{K,\Phi}^{(0)} + h_{\text{ST},\Phi}^{(0)} \quad (52)$$

is trivially zero due to the uniformity of Φ_0 and the rotational symmetry of the setup. In cylindrical coordinates this becomes

$$\dot{\Theta}_0 = \frac{\partial^2 \Theta_0}{\partial \rho'^2} + \frac{1}{\rho'} \frac{\partial \Theta_0}{\partial \rho'} - \frac{1}{2} \sin(2\Theta_0) + \omega_h \sin \Theta_0 = 0 \quad (53)$$

and

$$\omega_h = \left[\frac{\sigma' V(\rho')}{\alpha} - h'_Z \right]. \quad (54)$$

Equations (53) and (54) are identical to Eqs. (13)–(17) in [25]. As in [25], we search for stationary solutions in which the spin-torque term counteracts the damping. However, Hofer *et al.* [25] analyzed the case where the dissipative terms were a small perturbation; we do not make this assumption here.

Moving to the rotating frame allows us to ignore the precession of the system and gives us direct access to the slow dynamics in which the solutions to (53) correspond to dynamic equilibrium configurations which could be stable or unstable depending on the values of ω_h and current profile $\sigma' V$. As in [25], we define the current profile using the Heaviside step function \mathcal{H} , with a step at the nanocontact radius ρ^* : $V(\rho) = \mathcal{H}(\rho^* - \rho)$. The nontrivial solutions are identical to those found in [25] for the case $h_Z = 0$, $\nu = 0$, and $\rho^* = \rho_{\text{max}} \rightarrow \infty$. In [25] these are found to be unstable to small perturbations (see in particular Fig. 4 of that paper). In fact, our analysis indicates that these unstable solutions play an important physical role in the current context: they are the saddle configurations separating the two stable constant solutions $\Theta = 0$ and $\Theta = \pi$.

For intermediate nanocontact radii and current strength we obtained equilibrium configurations by performing a time integration of Θ using conservative droplet soliton profiles as the initial condition [43]. Final results are shown in Fig. 3. For low currents the magnetization relaxes toward $\Theta = 0$, but if the current magnitude passes a certain threshold σ_{crit} , then inside the nanocontact region the magnetization switches to $\Theta(\rho = 0) \rightarrow \pi$. Once the magnetization stops evolving, the domain wall separating the $\Theta = 0$ orientation from the $\Theta = \pi$ orientation is in the vicinity of the nanocontact's edge. The overall configuration inside the nanocontact corresponds to the stable droplet soliton for a given radius and current strength. These stable states are related to the stationary low-frequency droplet solitons of [24] which are described to

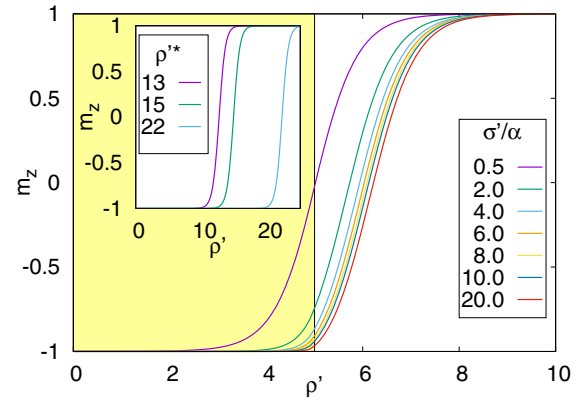


FIG. 3. Main figure: Stable droplet solitons for a variety of currents σ'/α (with $Q = 2$) for $\rho^* = 5$. In general, the transition region between $m_z = -1$ and $m_z = +1$ is approximately aligned with the nanocontact's edge. The asymmetry parameter $\nu = 0$ in these cases. The yellow region indicates the range of ρ' within the nanocontact region. Inset: m_z vs ρ' at $\sigma'/\alpha = 0.13$ for several nanocontact radii.

be stable against small displacements from the center of the nanocontact and are described as circular domain walls.

Notice that there will be an abrupt change in the precessional frequency at the nanocontact edge (since $\omega_{\text{ST}}|_{\rho \rightarrow \rho^{*-}} = \sigma'/\alpha'$, but $\omega_{\text{ST}}|_{\rho \rightarrow \rho^{*+}} = 0$). However, since $\Theta(\rho < \rho^*) \rightarrow \pi$ for very large currents, Φ becomes undefined. Additionally the Θ profile inside will merge nicely with the outside Θ profile of low-frequency stationary droplet solitons [24] which are of the form $\cos(\Theta) = \tanh(\rho - 1/\omega)$. The droplet soliton radii for the stable droplet solitons considered here will be larger than the radius of the nanocontact.

As we have already seen, given a spin-polarized current density, there is a reference frame rotating at frequency $\omega_{\text{ST}} = \frac{\sigma'}{\alpha'}$ for which the unstable solutions of (53) appear stationary. These are the saddle states between the configurations parallel and antiparallel to $\hat{\mathbf{m}}_p$. In the laboratory frame they precess with frequency ω_{ST} . This interpretation of Eq. (53) allows us to define a critical current above which reversal is guaranteed. That is, if we set $\rho^* = \infty$, and consider a small, global fluctuation $\delta\Theta$ away from $\Theta = 0$, we find

$$\dot{\Theta} \approx \left\{ -1 + \left[\frac{\sigma'}{\alpha} \left(\frac{1}{1+\nu} \right) - h'_Z \right] \right\} \delta\Theta > 0, \quad (55)$$

whenever

$$\frac{\sigma'}{\alpha} > \left(\frac{\sigma'}{\alpha} \right)_{\text{crit}} = (1+\nu)(h'_Z + 1). \quad (56)$$

For a finite nanocontact radius, the critical current must be larger and its meaning needs to be reevaluated. For finite ρ^* there will be a current magnitude for which the solution $\Theta = 0$ becomes unstable, but the reversed region does not expand much farther than the nanocontact radius: doing so would severely increase the exchange energy, by increasing the size of the reversed region and consequently the size of the domain wall that surrounds such fluctuations. As long as the domain wall is enclosed inside the nanocontact region any exchange energy cost will be compensated by a corresponding decrease in the value of the pseudopotential energy \mathcal{E}_{ST} . This

stops when the droplet soliton radius becomes comparable to ρ^* : further increases in the current density only serve to pin the magnetization closer to $\Theta = \pi$ but do not produce further growth of the droplet soliton radius.

In summary, if $\frac{\sigma'}{\alpha} > (\frac{\sigma'}{\alpha})_{\text{crit}}$, the solution $\Theta = 0$ is no longer stable, and a droplet soliton will be formed *necessarily* as the energy-minimizing configuration. When $\frac{\sigma'}{\alpha} < (\frac{\sigma'}{\alpha})_{\text{crit}}$, the solution $\Theta = 0$ is stable, and two nonuniform solutions of (53) exist: one is an energy minimum (stable droplet soliton), and the other is the saddle state (unstable droplet soliton) (these correspond to the stable and unstable branches shown in Fig. 4 of [25]). In the limit of infinite nanocontact radius all droplet solitons are saddles and the uniform $\Theta = \pi$ configuration is the stable state. (It has been suggested that these saddle states appear similar to experimentally realized spin-torque oscillator states observed in [50,51]).

Numerical solutions for the stationarity condition

To find solutions of Eq. (53) we use the BVP4C method from Matlab, as was done in [25]. The key difference is that we solve the equation for finite nanocontact radii, so the values of σ'/α need to be larger. We set $\rho'_{\text{max}} = 100$, fix the value of Θ at $\rho' = 0$, and let σ'/α be an eigenvalue parameter to be found numerically. We impose the following boundary conditions:

$$\left. \frac{\partial \Theta}{\partial \rho} \right|_{\rho=0} = 0, \quad \Theta(\rho = 0) = \Theta_{\text{max}}, \quad \Theta(\rho = \rho_{\text{max}}) = 0. \quad (57)$$

By performing this ‘‘poor man’s continuation’’ we can feed the solutions as initial guesses and solve for a wide range of parameters [43]. Every set of values ν , ρ^* , and Θ_{max} is associated with a value of σ'/α .

For comparison to the limit $\rho^* \rightarrow \infty$, we will identify ω_0 with the eigenvalue corresponding to the parameter set $\nu = 0$, $\rho^* = \rho_{\text{max}}$, and $\Theta = \Theta_{\text{max}}$. Keeping the same Θ_{max} but varying ν and ρ^* we find new values of σ'/α that have the same amplitude at the origin. In this way, we can compare the frequency that a finite nanocontact droplet soliton would have if it had the same amplitude Θ_{max} of the conservative droplet soliton.

In Fig. 4 we show results of this procedure for different values of ρ^* and fixed $\Theta_{\text{max}} = \frac{3}{4}\pi$. As the nanocontact area is reduced, a larger current is required to keep the fluctuations stationary. The profile is narrower in the radial direction. Because very strong currents are necessary for small nanocontact radii, the uniform $\Theta = 0$ state ceases to be metastable and the droplet soliton is sustained. For large radii, fluctuations of this amplitude require smaller currents but they represent energy saddles.

VII. OVERDAMPED DYNAMICS AND ACTIVATION BARRIERS

In this section we perform two types of simulations to confirm that solutions of Eq. (53) are indeed saddle configurations in the energy landscape. The first is a one-dimensional relaxation calculation which drops the precessional terms in Eqs. (22) and (23); the second is a full micromagnetic

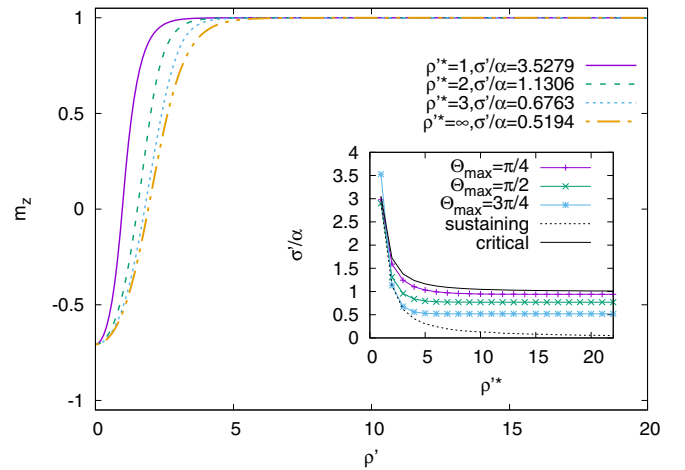


FIG. 4. Profiles of stationary fluctuations of amplitude $\Theta_{\text{max}} = 3\pi/4$ at different nanocontact radii ρ^* ($Q = 2$). As indicated in the legend a reduction in ρ^* must be accompanied by an increase on the current density. Inset: Currents required to maintain the fluctuation stationary. In these curves, $\nu = 0$. The area between the critical (solid black line) and the sustaining current (dotted black line) provides the range of currents in the region of bistability. These curves for critical and sustaining currents are obtained from the data of Fig. 9.

simulation using OOMMF [39] in which the spin-torque term \mathcal{E}_{ST} is added to the energy [43].

Both simulations approximate the same physical system, modeling a magnetic material with exchange constant $A = 13$ pJ/m and saturation magnetization $M_s = 8 \times 10^5$ A/m. To simplify the algebra, we selected an unphysically large K (so that $Q = 2$), but our approach will remain valid for more realistic values. The nanocontact diameter used is $r^* = 50$ nm ($\rho^* = 4.4$) and the thickness is $d = 1$ nm. The critical current, $I_c = \pi J_c r^{*2}$, for these parameters is 2.40 mA.

A. 1D relaxation

In the rotating reference frame, the long-term evolution can be captured using only the damping terms in Eqs. (22) and (23):

$$\dot{\Theta} = \alpha h_{\Theta}, \quad \dot{\Phi} = \alpha h_{\Phi}. \quad (58)$$

Here we assume uniform precessional states, i.e., $\Phi = \omega t$ and $\nabla \Phi = 0$, which guarantee that $h_{\Phi} = 0$ always. The time evolution of the droplet soliton profiles, $\Theta(\rho, t)$, contains enough information to verify whether a given configuration corresponds to a thermally activated transition state.

Starting with solutions of Eq. (53), we set $\alpha = 1$ and integrate $\dot{\Theta} = h_{\Theta}$ forward in time. We vary σ to find two values σ^+ and σ^- that satisfy two conditions: first, $0 < \sigma^+ - \sigma^- < 5 \times 10^{-5}$, and second, the initial profile relaxes to the uniform state for σ^- and to the stable droplet soliton for σ^+ . If the slope of the curve $\mathcal{E}_{\text{tot}}(t)$ is close to zero at $t = 0$, we take this as confirmation that the initial state constitutes the transition configuration for thermal activation [43].

Figure 5 illustrates this procedure. The difference of \mathcal{E}_{tot} values between the saddle droplet soliton and the uniform state (Δ^+) constitutes the barrier for droplet soliton creation; the difference between the saddle droplet soliton and the

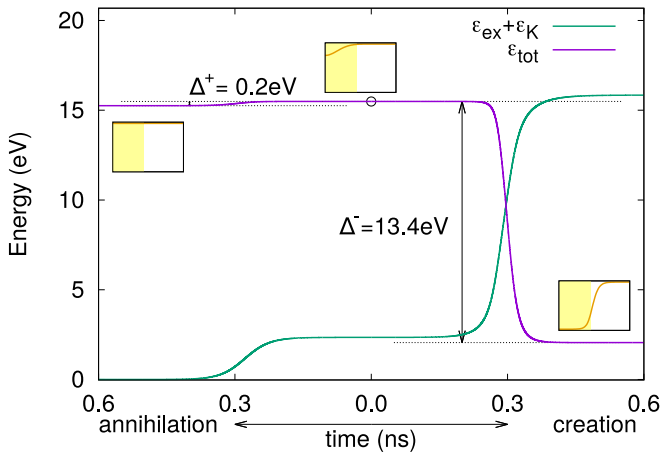


FIG. 5. Time evolution of the 1D overdamped dynamics. The initial state at time 0 is the droplet soliton saddle. Time increases from the center to the left for σ^- , corresponding to droplet annihilation, and from the center to the right for σ^+ corresponding to droplet creation. The spatial profiles, $m_z(\rho)$, of the final states are shown as in opposite margins and for the initial state in the center above the curve. The energy barriers for creation, Δ^+ , and annihilation, Δ^- , are shown in the figure with vertical arrows. The light yellow shade represents the area covered by the nanocontact. In this figure the initial profile is defined with $\omega_h = 0.9911$, $m_z(\rho = 0) = 0.52$. The two currents used for the time integration shown are $\sigma^- = 0.992218$ and $\sigma^+ = 0.992249$.

stable droplet soliton (Δ^-) constitutes the barrier for droplet soliton annihilation. Besides \mathcal{E}_{tot} , Fig. 5 also shows the energy terms excluding the spin-torque contribution ($\mathcal{E}_K - \mathcal{E}_{\text{ex}} = \mathcal{E}_{\text{tot}} - \mathcal{E}_{\text{ST}}$). It is clear from this figure that \mathcal{E}_{tot} is a better descriptor of thermal stability than the value without \mathcal{E}_{ST} .

In Sec. VII C, we will repeat this procedure systematically to find the energy barriers for different applied currents and nanocontact radii.

B. Overdamped micromagnetic simulations

We reproduce the qualitative features of the overdamped 1D dynamics with an equivalent system using OOMMF. To reduce computational time we drop the demagnetizing field term and set the crystalline anisotropy to $K_{\text{eff}} = \frac{K}{2} = \frac{\mu_0 M_s^2}{2}$, which in turn sets $Q = 2$. Because the precessional term cannot be dropped independently of the STT term, we allow for precession and set $\alpha = 1$. The disk has a diameter of 500 nm and we discretize the problem with 1 nm cubic cells.

The extension for spin-torque dynamics by Xiao *et al.* [52] was modified so that \mathcal{E}_{ST} was included as an energy term [43]. The dynamical part of the code was left unchanged and is based on Eq. (B1). The secondary spin-torque term, an additional curl-like term in the OOMMF extension, was set to zero. We set OOMMF's polarization and asymmetry to $P = 2$ and $\Lambda = 1.0$, respectively. This corresponds to $\nu = 0.0$ and fully efficient polarization.

We emphasize that our modification of the OOMMF code does not alter the dynamics; it is merely a bookkeeping change to incorporate the spin-torque pseudopotential into the energy. However, because the new term is relatively large we were

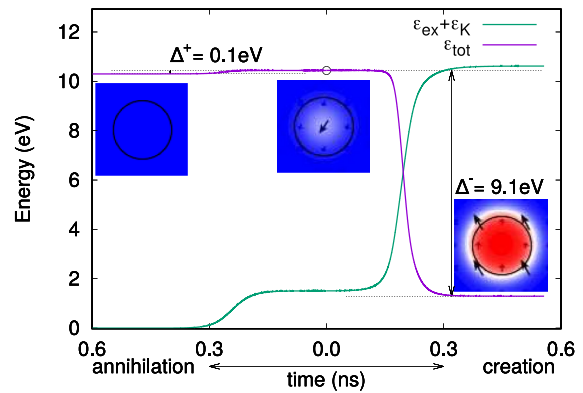


FIG. 6. Overdamped ($\alpha = 1$) OOMMF dynamics. The initial state is the droplet soliton saddle. The time evolution for creation and annihilation is the same as in Fig. 5. The spatial profiles, $m_z(x, y)$, of the final states are shown as in opposite margins and for the initial state in the center above the curve. The energy barriers for creation (Δ^+) and annihilation (Δ^-) are again depicted with vertical arrows. The area covered by the nanocontact is indicated by a white circle. In this figure the initial profile is defined with $\omega_h = 0.9911$, $m_z(\rho = 0) = 0.52$. The two currents used for the time integration shown are $I^- = 2.491$ mA and $I^+ = 2.492$ mA, so that $\sigma = 1.04$.

forced to relax the standard restriction that energy changes remain below a predetermined threshold. As a consequence, traces of energy evolution in time shown below appear noisy.

The initial magnetization is a 2D realization of the saddle configuration used in Sec. VII C. Successive simulations find two currents, I^+ and I^- , with difference $\delta I = I^+ - I^- = 10^{-4}$; the system evolves toward the uniformly magnetized state $m_z = 1$ for I^- and to the stable droplet soliton for I^+ . Results are shown in Figs. 6 and 7. These figures show qualitative agreement between the 1D model and the OOMMF micromagnetic simulations. In the latter the initial state is a saddle for a slightly larger current, $\sigma = 1.04$.

There are quantitative discrepancies between the two simulations that can be attributed to the fact that in the full micromagnetic simulations $\nabla\Phi$ may be nonzero. Furthermore, the slightly larger current of the OOMMF simulation widens the stable droplet soliton profile (see Fig. 8), changing all energy terms.

C. Energy barriers in the 1D approximation

Here we use the 1D overdamped approach to obtain the energy barriers for the droplet soliton at different scaled currents σ/α and nanocontact radii ρ^* .

The first step is to find the values of σ/α for different droplet soliton amplitudes and nanocontact radii ρ^* , which is done by solving Eq. (53). The resulting values are shown in Fig. 9. It can immediately be seen that as ρ^* increases, the infinite-nanocontact limit is rapidly approached. For the thermal stability calculations, the relevant segments are the solid parts of the curve; for those values the solutions represent saddle configurations which are then used as starting configurations for the overdamped simulations, as explained in Sec. VII A.

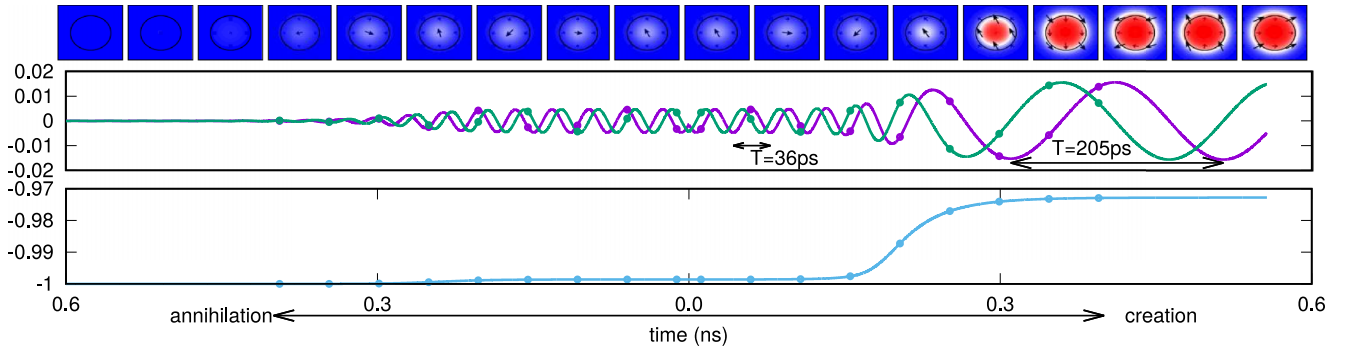


FIG. 7. Magnetization configurations of the overdamped ($\alpha = 1$) OOMMF dynamics, and spatially averaged magnetization components vs time. Both simulations start with the same initial configuration. As in the previous two figures, time evolution occurs to the left for $I^- = 2.491$ mA and to the right for $I^+ = 2.492$ mA. Points in the curve are associated with the figures in the top row. Consistent with expectations, the low-amplitude droplet soliton (saddle state) has a higher frequency than the large-amplitude droplet soliton (stable droplet soliton). The precessional frequency of each configuration can be estimated visually from this plot after rescaling time $\omega = \frac{2\pi}{\gamma_0 M_s T}$ giving $\omega_{\text{saddle}} = 0.9964$ and $\omega_{\text{stable}} = 0.1735$.

After simulating all saddle points the energy barriers were measured. Results are shown in Fig. 10. For large values of σ/α , the annihilation barrier Δ^- is close to linear, reflecting the fact that once the nanocontact region is saturated the profile remains unchanged, and \mathcal{E}_{ST} is roughly ω_{ST} multiplied by the nanocontact area. As σ/α is reduced [Fig. 10(b)], this quasilinearity is lost for smaller radii.

The creation barrier Δ^+ [Figs. 10(c) and 10(d)] has a singularity at $\sigma/\alpha = 0$ and decreases rapidly toward the critical current, consistent with expectations. As the nanocontact radius is reduced, the region of bistability is reduced and the barriers for droplet soliton creation grow.

VIII. PERTURBATION EXPANSIONS NEAR STATIONARY DYNAMICAL POINTS IN THE ROTATING FRAME

Small asymmetry parameter v , $\theta_f = 0$, $\theta_z = 0$

In this case, the fields are time independent, and we expect stationary states in the rotating frame. More generally, we can

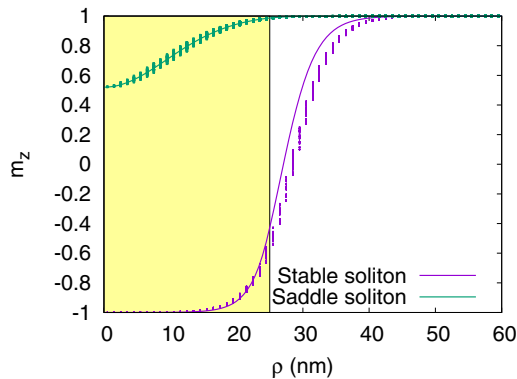


FIG. 8. Profiles of $\Theta(\rho)$ for overdamped micromagnetic simulations. Solid lines represent the droplet soliton profiles obtained from the overdamped 1D dynamics; the superimposed dots are obtained from OOMMF simulations. We attribute the small quantitative discrepancies partly to discretization effects and partly to the fact that exchange energy contributions from variations in the azimuthal direction are neglected in the 1D model.

expect a frequency shift $\omega^{(1)}$ that will be observable in both the static and the rotating frames. The first-order perturbations of the equations of motion obey

$$\dot{\Theta}_1 = h_{\Phi}^{(1)} + \alpha h_{\Theta}^{(1)}, \quad (59)$$

$$\dot{\Phi}_1 = -h_{\Theta}^{(1)} + \alpha h_{\Phi}^{(1)} - \frac{\sigma' V v}{2\alpha'} \sin 2\Theta_0. \quad (60)$$

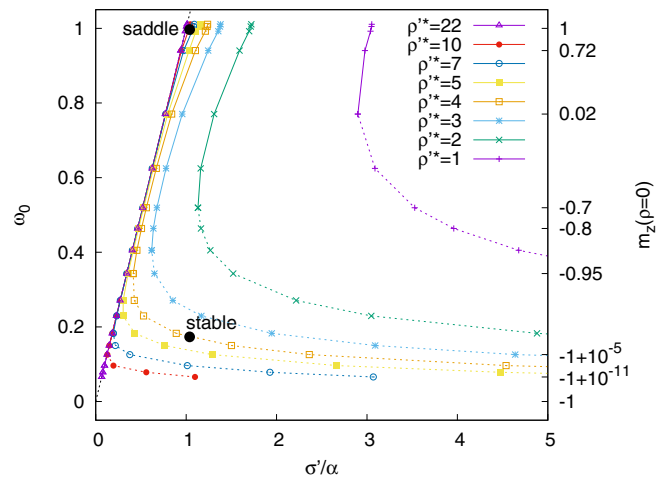


FIG. 9. Solutions of Eq. (53) for various m_z amplitudes at the origin: given $m_z(\rho = 0)$, the algorithm finds σ/α as an eigenvalue of (53). Along the left axis the frequency for the infinite nanocontact is shown; a dashed line of slope 1 depicts the infinite nanocontact limit. The different finite-nanocontact curves are superimposed over the infinite-nanocontact line already at moderate sizes. All curves are shown with two branches: the solid lines, where the slope is positive, represent the saddle states, and the dashed lines indicate the corresponding stable states. The critical current for a given nanocontact radius is the point at which the corresponding curve crosses the uniform state, i.e., where $m_z(\rho = 0) = 1$. The sustaining current for each radius corresponds to the vertex where the two branches meet. The filled black circles show the frequencies obtained from visual inspection of the OOMMF simulation; the points are expected to lie in the curve corresponding to $\rho^* = 4.4$.

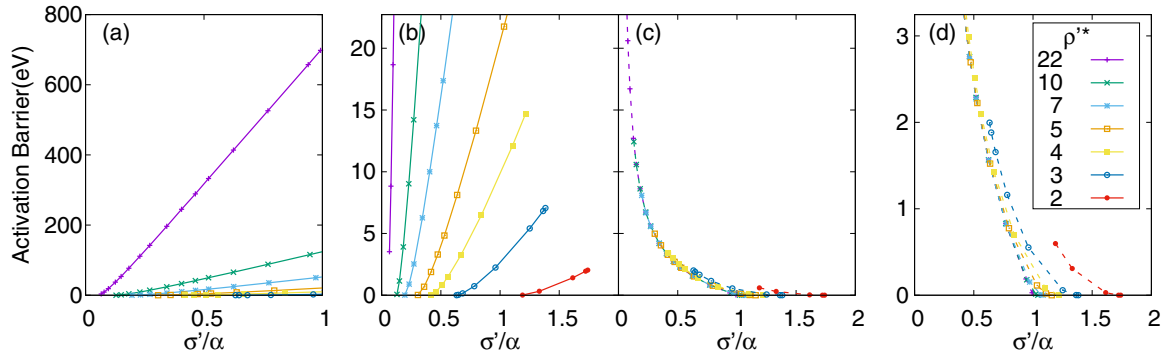


FIG. 10. Energy barrier dependence on current when $h = 0$, σ/α , calculated from the overdamped 1D dynamics with $h_Z = v = 0$ and different nanocontact radii ρ^* . (a), (b) Δ^- , barrier for droplet soliton annihilation. (c), (d) Δ^+ , barrier for droplet soliton creation. As shown, the values of Δ^+ are generally much smaller than Δ^- . To better illustrate the range of currents for which the barriers are Δ^+ and Δ^- , (b) and (c) are juxtaposed with the same axis scale.

As they are written above, both equations contain differential operators acting on Φ_1 and Θ_1 , but they can be decoupled at points of uniform precession about $\hat{\mathbf{m}}_p$, i.e., where $\dot{\Theta}_1 = 0$ and $\dot{\Phi}_1 = \omega^{(1)}$. This decoupling results in

$$h_{\Phi}^{(1)} = \left(\frac{\alpha}{1 + \alpha^2} \right) \left[\omega^{(1)} + \frac{\sigma' V v}{2\alpha'} \sin 2\Theta_0 \right] \quad (61)$$

and

$$h_{\Theta}^{(1)} = - \left(\frac{1}{1 + \alpha^2} \right) \left[\omega^{(1)} + \frac{\sigma' V v}{2\alpha'} \sin 2\Theta_0 \right]. \quad (62)$$

Thanks to our choice of coordinate system, a similar procedure can be performed to obtain decoupled equations to higher orders by substituting $h_{\Phi}^{(n)} = -\alpha h_{\Theta}^{(n)}$, from $\dot{\Theta}_n = 0$, into the equation for $\dot{\Phi}_n = \omega^{(n)}$. However, for now we restrict our discussion to the first-order case.

Setting θ_f and θ_Z to zero (cf. Appendix E) we obtain the first-order perturbation equation for Θ_1 :

$$h_{\Theta}^{(1)} = h_{\text{ex},\Theta}^{(1)} + h_{Z,\Theta}^{(1)} + h_{K,\Theta}^{(1)} + h_{\text{ST},\Theta}^{(1)}, \quad (63)$$

which after some manipulation simplifies to

$$L_{\Theta} \Theta_1 = - \frac{\omega^{(1)}}{(1 + \alpha^2)}, \quad (64)$$

with the Schrödinger operator L_{Θ} defined as

$$L_{\Theta} \equiv \left(-h'_Z + \frac{\sigma' V}{\alpha} \right) \cos \Theta_0 - \cos 2\Theta_0 + \nabla^2. \quad (65)$$

Similarly for Φ_1 ,

$$h_{\Phi}^{(1)} = h_{\text{ex},\Phi}^{(1)}, \quad (66)$$

$$L_{\Phi} \Phi_1 = \alpha' \left[\omega^{(1)} + \frac{\sigma' V v}{2\alpha'} \sin 2\Theta_0 \right],$$

with the corresponding Schrödinger operator

$$L_{\Phi} \equiv [(\nabla' \Theta_0)^2 - \cos \Theta_0 (\cos \Theta_0 - \omega_h)] + \nabla^2. \quad (67)$$

Since the two operators L_{Φ} and L_{Θ} are linear in Θ_1 and Φ_1 , the solution of Eqs. (64) and (66) must be linear combinations of their eigenfunctions:

$$\Theta_1 = \sum_n c_n \Theta_n^{(1)}, \quad \Phi_1 = \sum_n d_n \Phi_n^{(1)}, \quad (68)$$

where $\Theta_n^{(1)}$ and $\Phi_n^{(1)}$ are the basis vectors which satisfy

$$L_{\Theta} \Theta_n^{(1)} = \vartheta_n \Theta_n^{(1)}, \quad L_{\Phi} \Phi_n^{(1)} = \varphi_n \Phi_n^{(1)}, \quad (69)$$

and appropriate boundary conditions. With the solutions to this eigenproblem the stationary configuration is described by the set of coefficients $\{c_n, d_n\}$ which satisfy

$$\sum_n c_n \vartheta_n \Theta_n^{(1)} = - \frac{\omega^{(1)}}{(1 + \alpha^2)} \quad (70)$$

and

$$\sum_n d_n \varphi_n \Phi_n^{(1)} = \frac{\alpha \left[\omega^{(1)} + \frac{\sigma' V v}{2\alpha'} \sin 2\Theta_0 \right]}{1 + \alpha^2}. \quad (71)$$

In each of these equations, the right-hand side should be orthogonal to the kernel of the corresponding Schrödinger operator. It can be verified that the function $\varphi_0 = \sin \Theta_0$ belongs to the kernel of L_{Φ} , which provides a necessary condition for the existence of a coherent perturbation:

$$\omega^{(1)} = - \frac{\sigma' v \int_0^{\rho^*} \cos \Theta_0 \sin^2 \Theta_0 \rho d\rho}{\alpha' \int_0^{\infty} \sin \Theta_0 \rho d\rho}. \quad (72)$$

For this condition to be sufficient, we need to complement equation Eq. (66) with appropriate boundary conditions satisfied by φ_0 so that, based on the uniqueness and completeness theorem, it becomes the unique element of the kernel of L_{Φ} .

From the condition of regularity at the origin for Θ_0 we get

$$\left. \frac{\partial \varphi_0}{\partial \rho} \right|_{\rho=0} = \cos \Theta_0 \left. \frac{\partial \Theta_0}{\partial \rho} \right|_{\rho=0} = 0. \quad (73)$$

For the second boundary condition, we can postulate that the azimuthal angle far from the nanocontact is unperturbed:

$$\varphi(\rho \rightarrow \infty) = \sin \Theta_0 \Big|_{\rho \rightarrow \infty} = 0. \quad (74)$$

Using a similar procedure to that described in Sec. VI, we find the numerical solutions to the perturbation equations. The procedure is summarized as follows: for a given v a frequency shift is obtained using Eq. (72). We guess the initial values of the perturbation function at the origin [i.e., $\Phi_1(\rho = 0)$ and $\Theta_1(\rho = 0)$] and let the BVP4C method from Matlab find values for $\omega^{(1)}$ corresponding to those boundary conditions

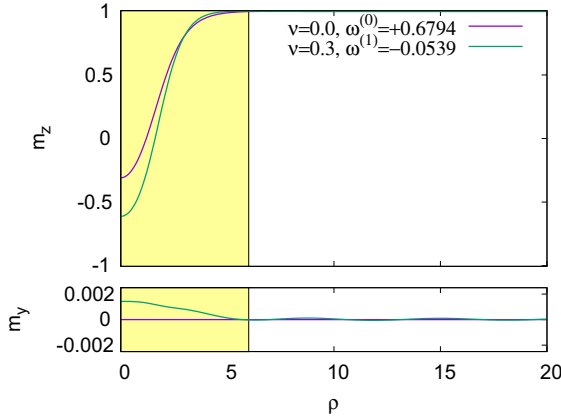


FIG. 11. The effect of finite asymmetry parameter ν in droplet soliton profiles: the amplitude, $\Theta(\rho)$, is increased and the azimuthal angle, $\Phi(\rho)$, is no longer constant. Here $m_y = \sin \Phi^{(1)} \sin(\Theta^{(0)} + \Theta^{(1)})$ and $\rho^* = 6.0$, $\alpha = 0.01$.

[43]. We iteratively tune $\Phi_1(\rho=0)$ and $\Theta_1(\rho=0)$ so that the output from Matlab approaches the value obtained from Eq. (72). This results in functions $\Phi_1(\rho)$ and $\Theta_1(\rho)$ with frequency shifts given by $\omega^{(1)}$. An example of such a solution is shown in Fig. 11.

These results show three effects that can be expected when the spin-torque-induced precessional frequency is rotationally symmetric but no longer radially uniform: a frequency shift ($\omega^{(1)} \neq 0$), an amplitude change ($\Theta^{(1)} \neq 0$), and a radially dependent buckling ($\Phi^{(1)} \neq 0$).

From the uniqueness argument we conclude that ρ^* , ν , σ , and α determine uniquely the shape of the perturbed droplet soliton and the new frequency of precession. It is clear that in a frame rotating with frequency $\omega_0 + \omega^{(1)}$ the droplet soliton appears stationary. Unfortunately, this situation occurs for a configuration for which $h_\Phi^{(1)} \neq 0$ and $h_\Theta^{(1)} \neq 0$. As a consequence, an estimate of the escape rates based solely on potential energy differences is no longer applicable. In this case, it is necessary to use the more general approach of Freidlin and Wentzell. We will return to this issue in Sec. IX and calculate the action for a specific class of fluctuational trajectories.

Nevertheless, we point out that the droplet soliton profiles found by solving Eqs. (64) and (66) have a well defined energy to first order in ν . This can be seen from Eq. (32), using the first-level expansion for $h_{ST,\Theta}$:

$$h_{ST,\Theta}^{(0)} \approx \frac{\sigma'V}{\alpha} \left[\sin \Theta_0 + \epsilon \Theta_1 \cos \Theta_0 + \frac{\nu \sin 2\Theta_0}{2} \right]. \quad (75)$$

Using $h_{ex,\Phi}^{(1)}$ from Eq. (61) we obtain the spin-torque power density:

$$\Xi^{(1)} = (h_{ST,\Theta}^0 + h_{ST,\Theta}^1) \times h_{ex,\Phi}^{(1)} \quad (76)$$

$$= h_{ST,\Theta}^0 \times h_{ex,\Phi}^{(1)} \quad (77)$$

$$= \frac{\sigma V}{\alpha} \sin \Theta_0 \times \frac{\alpha [\omega^{(1)} + \frac{\sigma'V\nu}{2\alpha'} \sin 2\Theta_0]}{1 + \alpha^2}. \quad (78)$$

Finally, integrating over the full disk we find

$$2\pi \int \Xi^{(1)} \rho d\rho = 0 \quad (79)$$

from the orthogonality condition Eq. (72). This means that for the droplet soliton profiles discussed above, the spin-torque power inflow in some regions of the disk is balanced by a spin-torque power outflow in another region. Since the fields are calculated only to first order, the total power dissipation, given by Eq. (50), is also zero.

IX. CONNECTION WITH FREIDLIN-WENTZELL THEORY

We next establish a connection between the pseudoenergy and the Freidlin-Wentzell action [30] for randomly perturbed dynamics. For simplicity, we use polar coordinates in the fixed laboratory frame, keeping track of the energy functions $\mathcal{E}_0 = \mathcal{E}_{ex} + \mathcal{E}_K + \mathcal{E}_Z$ and $\mathcal{E}_{tot} = \mathcal{E}_0 + \mathcal{E}_{ST}$. Writing the Landau-Lifshitz operator and its inverse as

$$\mathbb{L}_{\Theta,\Phi} = \begin{pmatrix} \alpha & 1 \\ -\frac{1}{\sin \Theta} & \frac{\alpha}{\sin \Theta} \end{pmatrix}, \quad \mathbb{L}_{\Theta,\Phi}^{-1} = \frac{\begin{pmatrix} \alpha & -\sin \Theta \\ 1 & \alpha \sin \Theta \end{pmatrix}}{1 + \alpha^2}, \quad (80)$$

the equation of motion in the presence of noise can be written

$$\dot{\mathbf{m}}_{\Theta,\Phi} - \mathbb{L}_{\Theta,\Phi} \mathbf{h}_{tot} - \mathbf{f} = \sqrt{2\eta} \mathbb{L}_{\Theta,\Phi} \dot{\mathbf{W}}, \quad (81)$$

where three two-component vectors have been introduced: $\dot{\mathbf{m}}_{\Theta,\Phi} = \{\dot{\Theta}, \dot{\Phi}\}$, $\mathbf{f} = \{0, \omega_{ST} \frac{1}{1+\nu \cos \Theta}\} = \{\frac{1}{\sin \Theta} \frac{\delta \mathcal{E}_{ST}}{\delta \Phi}, -\frac{1}{\sin \Theta} \frac{\delta \mathcal{E}_{ST}}{\delta \Theta}\}$, and $\mathbf{h}_{tot} = \{-\frac{\delta \mathcal{E}_{tot}}{\delta \Theta}, -\frac{1}{\sin \Theta} \frac{\delta \mathcal{E}_{tot}}{\delta \Phi}\}$.

The deterministic part of Eq. (81) can be simplified using the vector $\mathbf{b}_{\Theta,\Phi} \equiv \mathbb{L}_{\Theta,\Phi} \mathbf{h}_{tot} + \mathbf{f}$, resulting in the equation

$$\mathbb{L}_{\Theta,\Phi}^{-1} [\dot{\mathbf{m}}_{\Theta,\Phi} - \mathbf{b}_{\Theta,\Phi}] = \sqrt{2\eta} \dot{\mathbf{W}}. \quad (82)$$

The Freidlin-Wentzell action per unit thickness is

$$S = \iiint \mathcal{L} \rho d\rho d\phi dt, \quad (83)$$

where

$$\mathcal{L} = \frac{1}{2} \mathbb{A}_{ii}^{-1} [\dot{\mathbf{m}}_{\Theta,\Phi} - \mathbf{b}_{\Theta,\Phi}]_i^2 \quad (84)$$

is the Freidlin-Wentzell Lagrangian and

$$\mathbb{A}^{-1} = (\mathbb{L}_{\Theta,\Phi}^{-1})^T \mathbb{L}_{\Theta,\Phi}^{-1} = \begin{pmatrix} 1 & 0 \\ 0 & \sin^2 \Theta \end{pmatrix} \quad (85)$$

is the inverse of the diffusion tensor.

Because the white noise modeling thermal effects do not destroy the global rotational symmetry of the magnetization, we can integrate out the azimuthal coordinates, leading to the reduced action

$$S_\rho = \iint \mathcal{L}_\rho d\rho dt \quad (86)$$

with

$$\mathcal{L}_\rho(h_\Theta, h_\Phi, \dot{\Phi}, \dot{\Theta}; t, \rho) = \frac{2\pi\rho}{2} \mathbb{A}_{ii}^{-1} [\dot{\mathbf{m}}_{\Theta,\Phi} - \mathbf{b}_{\Theta,\Phi}]_i^2. \quad (87)$$

Because of the rotational symmetry we can write

$$\mathbb{A}_\rho^{-1} = (\mathbb{L}_{\Theta,\Phi}^{-1})^T \mathbb{L}_{\Theta,\Phi}^{-1} = \begin{pmatrix} \rho & 0 \\ 0 & \rho \sin^2 \Theta \end{pmatrix} \quad (88)$$

$$= (\sqrt{2\pi\rho})^2 \mathbb{A}^{-1}. \quad (89)$$

The extra radial factor accounts for the fact that coherent thermal fluctuations for annuli of radius ρ and width $d\rho$ become rarer as ρ increases. This can be interpreted as follows: if the sample is discretized in infinitesimal segments of $d\mathcal{V}$ and the thermal field on each segment has standard deviation h_{th} , then the averaged field fluctuation on the annulus as a whole grows only as $h_\rho = \sqrt{\rho} h_{\text{th}}$. At any instant of time, a coherent fluctuation of unit size observed at radius ρ requires a thermal energy density proportional to $h_\rho^2 = \rho h_{\text{th}}^2$, thereby decreasing in likelihood as ρ increases. The Freidlin-Wentzell Lagrangian is a measure of such thermal energy and therefore grows proportionally to the volume.

We will calculate the action for two specific translation paths \mathbf{m}_\downarrow , \mathbf{m}_\uparrow that we now define. First we separate the damping from the precessional part of the Landau-Lifshitz operator:

$$\mathbb{L}_{\Theta,\Phi} = \mathbb{L}_{\Theta,\Phi}^\alpha + \mathbb{L}_{\Theta,\Phi}^\gamma, \quad (90)$$

$$\mathbb{L}_{\Theta,\Phi}^\alpha = \alpha \begin{pmatrix} 1 & 0 \\ 0 & \frac{1}{\sin \Theta} \end{pmatrix}, \quad \mathbb{L}_{\Theta,\Phi}^\gamma = \begin{pmatrix} 0 & 1 \\ -\frac{1}{\sin \Theta} & 0 \end{pmatrix}, \quad (91)$$

which allows us to write the (deterministic) drift field as

$$\mathbf{b}_{\Theta,\Phi} = \mathbb{L}_{\Theta,\Phi}^\alpha \mathbf{h}_{\text{tot}} + \mathbb{L}_{\Theta,\Phi}^\gamma (\mathbf{h}_{\text{tot}} + \mathbf{h}_{\text{ST}}). \quad (92)$$

The paths of interest are then defined as follows:

$$\dot{\mathbf{m}}_\downarrow = \mathbf{b}_{\Theta,\Phi} = \mathbb{L}_{\Theta,\Phi}^\alpha \mathbf{h}_{\text{tot}} + \mathbb{L}_{\Theta,\Phi}^\gamma (\mathbf{h}_{\text{tot}} + \mathbf{h}_{\text{ST}}) \quad (93)$$

and

$$\begin{aligned} \dot{\mathbf{m}}_\uparrow &= \mathbf{b}_{\Theta,\Phi} - 2\mathbb{L}_{\Theta,\Phi}^\alpha \mathbf{h}_{\text{tot}} \\ &= -\mathbb{L}_{\Theta,\Phi}^\alpha \mathbf{h}_{\text{tot}} + \mathbb{L}_{\Theta,\Phi}^\gamma (\mathbf{h}_{\text{tot}} + \mathbf{h}_{\text{ST}}). \end{aligned} \quad (94)$$

Our choice of fluctuational paths is motivated as follows: one of the two pieces of the drift field, $\mathbb{L}_{\Theta,\Phi}^\alpha \mathbf{h}_{\text{tot}}$, is curl-free and so can be derived as the gradient of a potential. The other piece, $\mathbb{L}_{\Theta,\Phi}^\gamma (\mathbf{h}_{\text{tot}} + \mathbf{h}_{\text{ST}})$, is divergenceless and so can be represented as the curl of a (separate) potential function. We choose the fluctuational trajectory so that the nonzero-curl term does not contribute to the Freidlin-Wentzell action.

The action for the ‘‘downhill’’ path \mathbf{m}_\downarrow is zero, since $\dot{\mathbf{m}}_\downarrow$ runs parallel to the deterministic field. The Lagrangian for the ‘‘uphill’’ path \mathbf{m}_\uparrow is

$$\begin{aligned} \mathcal{L} &= \frac{1}{2} \mathbb{A}_{ii}^{-1} [\dot{\mathbf{m}}_\uparrow - \mathbf{b}_{\Theta,\Phi}]_i^2 \\ &= \frac{1}{2} \mathbb{A}_{ii}^{-1} [\dot{\mathbf{m}}_\uparrow - \mathbb{L}_{\Theta,\Phi}^\alpha \mathbf{h}_{\text{tot}} - \mathbb{L}_{\Theta,\Phi}^\gamma (\mathbf{h}_{\text{tot}} + \mathbf{h}_{\text{ST}})]_i^2 \\ &= \frac{1}{2} \mathbb{A}_{ii}^{-1} [\dot{\mathbf{m}}_\uparrow + \mathbb{L}_{\Theta,\Phi}^\alpha \mathbf{h}_{\text{tot}} - \mathbb{L}_{\Theta,\Phi}^\gamma (\mathbf{h}_{\text{tot}} + \mathbf{h}_{\text{ST}})]_i^2 \\ &\quad - 2[\mathbb{L}_{\Theta,\Phi}^\alpha \mathbf{h}_{\text{tot}}]^T \mathbb{A}_{ii}^{-1} [\dot{\mathbf{m}}_\uparrow - \mathbb{L}_{\Theta,\Phi}^\gamma (\mathbf{h}_{\text{tot}} + \mathbf{h}_{\text{ST}})] \\ &= -2[\mathbb{L}_{\Theta,\Phi}^\alpha \mathbf{h}_{\text{tot}}]^T \mathbb{A}_{ii}^{-1} [\dot{\mathbf{m}}_\uparrow - \mathbb{L}_{\Theta,\Phi}^\gamma (\mathbf{h}_{\text{tot}} + \mathbf{h}_{\text{ST}})] \\ &= -2\mathbf{h}_{\text{tot}}^T (\mathbb{L}_{\Theta,\Phi}^\alpha)^T \mathbb{A}_{ii}^{-1} \dot{\mathbf{m}}_\uparrow \end{aligned}$$

$$\begin{aligned} &+ 2\mathbf{h}_{\text{tot}}^T (\mathbb{L}_{\Theta,\Phi}^\alpha)^T \mathbb{A}_{ii}^{-1} \mathbb{L}_{\Theta,\Phi}^\gamma (\mathbf{h}_{\text{tot}} + \mathbf{h}_{\text{ST}}) \\ &= \mathcal{L}_0 + \mathcal{L}_{\text{ST}}. \end{aligned} \quad (95)$$

The first term is

$$\begin{aligned} \mathcal{L}_0 &= -2\mathbf{h}_{\text{tot}}^T (\mathbb{L}_{\Theta,\Phi}^\alpha)^T \mathbb{A}_{ii}^{-1} \dot{\mathbf{m}}_\uparrow \\ &= +2\alpha \rho \left[\frac{\delta \mathcal{E}_{\text{tot}}}{\delta \Theta} \dot{\Theta} + \frac{\delta \mathcal{E}_{\text{tot}}}{\delta \Phi} \dot{\Phi} \right], \end{aligned} \quad (96)$$

which, after integrating over time and space, gives

$$S_0 = \iint \mathcal{L}_0 d\rho dt = 2\Delta E_{\text{tot}}. \quad (97)$$

The second term, using $\mathbf{h}_{\text{ST}} = \{-\frac{\delta \mathcal{E}_{\text{ST}}}{\delta \Theta}, 0\}$, gives

$$\mathcal{L}_{\text{ST}} = 2\alpha h_{\text{ex},\Phi} h_{\text{ST},\Theta} = 2\alpha \rho \Xi. \quad (98)$$

Therefore, integration over time and space gives the spin-torque-induced action

$$S_{\text{ST}} = \iint \mathcal{L}_{\text{ST}} = 2\alpha \iint \Xi \rho d\rho dt. \quad (99)$$

As described before, the total power input in the droplet soliton configurations described satisfies

$$\int \Xi \rho d\rho = 0. \quad (100)$$

So, combining Eqs. (97)–(100) for escape trajectories which include configurations having zero spin-torque-induced energy flow, the Freidlin-Wentzell action is simply twice the energy difference between the initial and final states, as is the case in simpler systems with gradient drift fields arising from a potential.

X. DISCUSSION

In this paper we have studied the thermal stability of magnetic droplet solitons which are linearly stable against the drift instability [25,27]. Taking advantage of the rotational symmetry, we transform the problem to a reference frame that rotates with the droplet soliton, thereby simplifying the problem. We introduced a pseudopotential that can incorporate the nongradient spin-torque terms, allowing us to analyze the problem using the Kramers approach to computing reversal rates. Numerical simulations of the dynamical LLGS equations demonstrate that the system indeed evolves toward one or another (depending on initial conditions) of the pseudopotential minima.

Our central result is summarized in Fig. 10, which shows the activation barriers for thermally (or other noise) induced escape from the droplet soliton to the uniform magnetization state, for a variety of nanocontact radii and spin-torque-inducing currents. As a function of current, barriers grow faster for larger radii.

We next discuss possible scenarios in which these results can be generalized, and discuss the model’s limitations, and in particular situations where it breaks down.

Large Oersted fields are known to induce modulational instabilities that force the droplet soliton out of the nanocontact region at relatively short times [10,26]. For this regime, thermal activation over a barrier is irrelevant since the droplet

soliton decays before thermal processes can play any role. But even for moderate currents the Oersted field introduces a time-harmonic perturbation of the dynamics that we have omitted. A continuous generalization of the Poincaré-Melnikov method is worth pursuing to incorporate fields with in-plane components. This will be the focus of future work.

In our approach, we initially assumed that the magnetization has a common frequency of precession with $\nabla\Phi = 0$. This requires $\nu = 0$. For $\nu \neq 0$, to first order the spin-torque dynamical term produces exchange-driven shearing of the magnetization, resulting in a nonuniform Φ . As shown in Fig. 11, three main effects are observed: first, a distortion of the $\Theta(\rho)$ profile of the droplet soliton; second, a frequency shift common to all reference frames; and third, a “buckling” of the azimuthal angle $\Phi(\rho) \neq 0$.

An extreme situation involved with this shearing occurs for small nanocontact radii. Inside the nanocontact the spin-torque-induced precessional term is proportional to σ'/α , and outside it is zero. Because the two regions precess at different rates, large exchange torques are created at the nanocontact edge. The interfacial shear at the boundary between the two regions will produce similar effects to those found for $\nu = 0$, and can be neglected if $\sin\theta \approx 0$ at the nanocontact edge. This is the case for small and large amplitude droplet solitons, or for large ρ^* . However, as $\rho^* \rightarrow 0$ this shearing becomes important and the spin-torque energy might “leak” beyond the nanocontact region resulting in spatial modulation of the magnetization far beyond the nanocontact region (see [53] for examples of such modulation). For this scenario, the total energy of the system will continue to increase as oscillations develop far from the nanocontact. However, as we discussed in the main text of the paper, the limit $\rho^* \rightarrow \infty$ is valid for radii that are experimentally relevant.

As noted in the introduction, even in the region of the current/field phase diagram where the droplet soliton is linearly stable to the drift instability, thermal activation over a barrier can still eject the droplet soliton from the nanocontact region. Numerical estimates of this thermally induced ejection have been provided in [27], where two mechanisms for thermally activated droplet soliton annihilation were considered: “noise-induced damping,” which corresponds to the droplet soliton decay mechanism considered in this paper, and ejection via drift instability. Because our analysis mostly considers different regions of the parameter space from those addressed in [27], a direct comparison between our results and theirs is not possible at the present time. We expect this to be a topic for future study. Nevertheless, as a first step we summarize below the differences in parameters chosen so that the difference in the regions of parameter space studied in the two papers is clarified.

The droplet soliton profile configurations used in [27] are restricted to the case of small σ and α , while this constraint is not present in the current work. Figure 9 summarizes the result that the conservative droplet soliton profiles correspond to saddle configurations in the $\rho^* \rightarrow \infty$ limit. The procedure we have followed allows us to find droplet soliton profiles for saddle states at arbitrary values of ρ^* , and also at $\nu \neq 0$ when $h_z = 0$.

Reference [27] examines mostly cases where $h_z > 1.0$ and the applied current is moderate-to-large. Our discussion

focuses instead on zero or small fields (cf. Fig. 10), given that the low-field regime provides the widest range of droplet soliton stability with respect to applied current (cf. Fig. 2 of [26]). Turning on an external field has several effects: first, it produces a shift of the droplet soliton frequency with respect to the current, similar to that observed for conservative droplet solitons [24]. This has the effect of reducing the droplet soliton amplitude. More relevant to the present discussion is that it lowers the activation barrier for both modes of droplet soliton decay. In addition, [27] found that increasing the current in large fields facilitates escape via the drift instability.

It is important to note that the formulation used for STT both in our paper and in the sequence of papers leading up to [24] assumes a fixed-layer polarization $\hat{\mathbf{m}}_p$ perpendicular to the film plane [24–26,54]. This setup differs from actual experiments that typically use an easy-plane polarization layer [3,28,55,56]. As a consequence, large external fields are needed to reorient $\hat{\mathbf{p}}$ along \mathbf{n}_\perp in order to approximate the highly symmetric case. Such large fields reduce the range of currents in which the stationary droplet soliton is stable against drift, as discussed in [27].

Because our methods exploit the presence of circular symmetry, and used $\hat{\mathbf{p}}$ as a privileged direction for the polar axes to define the rotational reference frame, our predictions are relevant to a so-called “all-perpendicular” device (i.e., $\hat{\mathbf{p}} \parallel \mathbf{n}_\perp$) [11].

We now estimate droplet soliton lifetimes in the presence of thermal noise due to the decay mechanism described in this paper, based on data from Fig. 10. We emphasize that these estimates are based on the leading-order asymptotics, i.e., the action barriers which determine the exponential Arrhenius factor, of the activation times for droplet soliton decay. The prefactors, which correspond to subdominant terms, are estimated below. We caution that these transition times should not be confused with deterministic creation and annihilation times, which are on the nanosecond timescale.

We assume a Co/Ni free layer in zero field with magnetization $\mu_0 M_s = 0.9$ T and $H_K = 1.35$ T ($Q = 1.5$), as in [55]. We assume $A = 13$ pJ/m and $\alpha = 0.01$. With these parameters, we examine the droplet soliton stability in a nanocontact of scaled radius $\rho^* = 5$ ($r^* = 22.5$ nm). The sustaining current is $I_{\min} = 2.3$ mA and the critical current is $I_{\max} = 9.0$ mA. If we assume an attempt rate given by $f_0 = \omega_{ST}\alpha = \sigma\gamma_0 M_s$ we can estimate lifetimes using $f_0^{-1} e^{\frac{\Delta}{k_B T}}$ at room temperature $T = 300$ K. With a current of 2.8 mA the mean lifetime of a droplet soliton in the presence of thermal noise is approximately 12 minutes ($\Delta^- \approx 26k_B T$) while the uniform state is very stable ($\Delta^+ \approx 127k_B T$). For a larger current of 6.5 mA, the droplet soliton generation time is slightly under 2 minutes ($\Delta^+ \approx 25k_B T$). Once nucleated, however, it is very stable ($\Delta^- \approx 190k_B T$). In a highly symmetric experimental setup, the signal from the resonant frequency of the droplet soliton is very weak, and one must rely on magnetoresistance measurements to determine the presence or absence of a droplet soliton.

ACKNOWLEDGMENTS

The authors are grateful to Andy Kent for useful discussions and comments on the manuscript. We are also grateful to Mark Hoefer for a useful correspondence in the early

stages of this work, and to an anonymous referee for the suggestion that the saddle states discussed in this paper appear similar to experimentally observed spin-torque oscillator states. This research was supported in part by US National Science Foundation Grant No. DMR 1610416 (D.L.S.) and the National Science Centre Poland under OPUS funding Grant No. 2019/33/B/ST5/02013 (G.D.C.-O.).

APPENDIX A: EFFECTIVE FIELD AND BOUNDARY CONDITIONS

Consider a quasi-2D system with nanocontact radius ρ^* , free-layer radius ρ_{\max} , surface area Ω , and thickness d . Using the Kohn-Slaskov approximation [57], we write the micro-magnetic energy as

$$\frac{E}{d} = \int_{\Omega} \left\{ A |\nabla \mathbf{m}|^2 - \left(K_S - \frac{\mu_0 M_s^2}{2} \right) m_z^2 - \mu_0 M_s \mathbf{m} \cdot \mathbf{H}_0 \right\} d^2 \mathbf{r} + K_{\text{edge}} \oint_{\partial \Omega} (\mathbf{m} \cdot \mathbf{n}_{\parallel})^2 d\mathbf{r}, \quad (\text{A1})$$

where $K_{\text{edge}} = \frac{\mu_0 M_s^2 d}{4\pi} |\ln(\frac{t}{2R})|$, \mathbf{n}_{\parallel} is the in-plane vector perpendicular to the sample's edge, and the field $\mathbf{H}_0 = \mathbf{H}_{\text{oe}} + \mathbf{H}_Z$ includes external and Oersted contributions.

Varying both sides of Eq. (A1) yields

$$\frac{\delta E}{d} = \int_{\Omega} 2A (\nabla \mathbf{m}) \cdot (\nabla \delta \mathbf{m}) d^2 \mathbf{r} \quad (\text{A2})$$

$$- \int_{\Omega} 2 \left(K_S - \frac{\mu_0 M_s^2}{2} \right) (\hat{\mathbf{z}} \cdot \mathbf{m}) (\hat{\mathbf{z}} \cdot \delta \mathbf{m}) d^2 \mathbf{r} \quad (\text{A3})$$

$$- \int_{\Omega} \mu_0 M_s \mathbf{H}_0 \cdot \delta \mathbf{m} d^2 \mathbf{r} \quad (\text{A4})$$

$$+ 2 \oint_{\partial \Omega} [K_{\text{edge}} (\mathbf{m} \cdot \mathbf{n}_{\parallel})] \delta \mathbf{m} \cdot \mathbf{n} d\mathbf{r}. \quad (\text{A5})$$

The first term contains derivatives of $\delta \mathbf{m}$ and corresponds to the effects of exchange. Following Brown and Miltat [58] we use the relation $\nabla \cdot (\nabla \mathbf{m} \cdot \delta \mathbf{m}) = (\nabla^2 \mathbf{m}) \delta \mathbf{m} + \nabla \mathbf{m} \cdot \nabla \delta \mathbf{m}$ to integrate by parts, yielding

$$\int_{\Omega} (\nabla \mathbf{m}) \cdot (\nabla \delta \mathbf{m}) = \int_{\Omega} \nabla \cdot (\nabla \mathbf{m} \cdot \delta \mathbf{m}) d^2 \mathbf{r} - \int_{\Omega} (\nabla^2 \mathbf{m}) \delta \mathbf{m} d^2 \mathbf{r}. \quad (\text{A6})$$

Using Gauss' theorem to rewrite the first term on the RHS yields

$$\int_{\Omega} (\nabla \mathbf{m}) \cdot (\nabla \delta \mathbf{m}) = \oint_{\partial \Omega} \left(\frac{\partial \mathbf{m}}{\partial \mathbf{n}_{\parallel}} \cdot \delta \mathbf{m} \right) d\mathbf{r} - \int_{\Omega} (\nabla^2 \mathbf{m}) \delta \mathbf{m} d^2 \mathbf{r}. \quad (\text{A7})$$

Rearranging this variational expression into bulk and surface terms we get

$$\frac{\delta E}{d} = \int_{\Omega} \left[-2A (\nabla^2 \mathbf{m}) - 2\hat{\mathbf{z}}_L \left(K_S - \frac{\mu_0 M_s^2}{2} \right) (\hat{\mathbf{z}}_L \cdot \mathbf{m}) + \mu_0 M_s \mathbf{H}_0 \right] \delta \mathbf{m} d^2 \mathbf{r} + 2 \oint_{\partial \Omega} \left[K_{\text{edge}} (\mathbf{m} \cdot \mathbf{n}_{\parallel}) (\mathbf{n}_{\parallel} \cdot \delta \mathbf{m}) + A \frac{\partial \mathbf{m}}{\partial \mathbf{n}_{\parallel}} \cdot \delta \mathbf{m} \right] d\mathbf{r}. \quad (\text{A8})$$

From the bulk integral we obtain the effective field

$$\mathbf{h}_{\text{eff}} = -\frac{1}{\mu_0 M_s^2} \frac{\delta \mathcal{E}}{\delta \mathbf{m}} = l^2 (\nabla^2 \mathbf{m}) + (Q - 1) (\hat{\mathbf{z}}_L \cdot \mathbf{m}) \hat{\mathbf{z}}_L + \mathbf{h}_0, \quad (\text{A9})$$

where $Q = 2K_S / (\mu_0 M_s^2) > 1$ is the (dimensionless) magnitude of the crystal anisotropy field.

Turning to the surface integral

$$\oint_{\partial \Omega} \left[K_{\text{edge}} (\mathbf{m} \cdot \mathbf{n}_{\parallel}) (\mathbf{n}_{\parallel} \cdot \delta \mathbf{m}) + A \frac{\partial \mathbf{m}}{\partial \mathbf{n}_{\parallel}} \cdot \delta \mathbf{m} \right] d\mathbf{r}, \quad (\text{A10})$$

we rewrite the magnetization variation as $\delta \mathbf{m} = \delta \theta \times \mathbf{m}$,

$$\oint_{\partial \Omega} \left[K_{\text{edge}} (\mathbf{m} \cdot \mathbf{n}_{\parallel}) \mathbf{n}_{\parallel} \cdot (\delta \theta \times \mathbf{m}) + A \frac{\partial \mathbf{m}}{\partial \mathbf{n}_{\parallel}} \cdot (\delta \theta \times \mathbf{m}) \right] d\mathbf{r}, \quad (\text{A11})$$

which shows that any variation conserves the norm of \mathbf{m} .

Finally, using the cyclic permutation of the triple vector product gives the surface integral contribution to the energy variation,

$$\oint_{\partial \Omega} \left[K_{\text{edge}} (\mathbf{m} \cdot \mathbf{n}_{\parallel}) (\mathbf{m} \times \mathbf{n}_{\parallel}) + A \left(\mathbf{m} \times \frac{\partial \mathbf{m}}{\partial \mathbf{n}_{\parallel}} \right) \right] \delta \theta d\mathbf{r}. \quad (\text{A12})$$

For this contribution to be extremal, it must be zero independently of $\delta \theta$, so

$$K_{\text{edge}} (\mathbf{m} \cdot \mathbf{n}_{\parallel}) (\mathbf{m} \times \mathbf{n}_{\parallel}) + A \left(\mathbf{m} \times \frac{\partial \mathbf{m}}{\partial \mathbf{n}_{\parallel}} \right) = 0. \quad (\text{A13})$$

Cross-multiplying with \mathbf{m} gives the boundary condition,

$$\frac{K_{\text{edge}}}{A} (\mathbf{m} \cdot \mathbf{n}_{\parallel}) [(\mathbf{m} \cdot \mathbf{n}_{\parallel}) \mathbf{m} - \mathbf{n}_{\parallel}] = \frac{\partial \mathbf{m}}{\partial \mathbf{n}_{\parallel}}. \quad (\text{A14})$$

Since the vector normal to the surface lies along $\hat{\rho}$ we get

$$\frac{K_{\text{edge}}}{A} (\mathbf{m} \cdot \hat{\rho}) [(\mathbf{m} \cdot \hat{\rho}) \mathbf{m} - \hat{\rho}] = \frac{\partial \mathbf{m}}{\partial \rho}, \quad (\text{A15})$$

so, recalling that Θ is the angle the magnetization makes with respect to the normal to the free-layer disk, we have

$$\frac{K_{\text{edge}}}{A} \sin \Theta (\mathbf{m} \sin \Theta - \hat{\rho}) = \frac{\partial \mathbf{m}}{\partial \rho}. \quad (\text{A16})$$

For rescaling in a way compatible with Eq. (12) we need to use $K_{\text{edge}} = K'_{\text{edge}} \sqrt{Q - 1}$.

The boundary condition (A16) is compatible with the cases we have been studying: if we set $\Theta = 0$ at ρ_{\max} then $\frac{\partial \mathbf{m}}{\partial \rho}$

must also be zero at ρ_{\max} . That is, the homogeneous Dirichlet boundary condition enforces the free boundary condition.

However, an expression for more general scenarios is also possible: if $\Theta \neq 0$ at the boundary, the proper boundary condition would be

$$\frac{\partial \Theta}{\partial \rho} = -\frac{K_{\text{edge}}}{2A} \sin(2\Theta) \cos^2(\Phi - \phi), \quad (\text{A17})$$

$$\frac{\partial \Phi}{\partial \rho} = \frac{K_{\text{edge}}}{2A} \sin[2(\Phi - \phi)]. \quad (\text{A18})$$

These boundary conditions are important for studying dynamical skyrmions [5,59].

APPENDIX B: DERIVATION OF THE LANDAU-LIFSHITZ-SLONCZEWSKI EQUATION

The magnetization dynamics in the presence of spin-polarized currents are obtained by adding the Slonczewski spin torque to the Landau-Lifshitz-Gilbert equation [60]:

$$\dot{\mathbf{m}} = \alpha \mathbf{m} \times \dot{\mathbf{m}} + \gamma_0 M_s \left[\sigma V \frac{\mathbf{m} \times \mathbf{m} \times \hat{\mathbf{m}}_p}{1 + \nu \mathbf{m} \cdot \hat{\mathbf{m}}_p} - \mathbf{m} \times \mathbf{h}_{\text{eff}} \right]. \quad (\text{B1})$$

Cross-multiplying Eq. (B1) with \mathbf{m} , substituting the result back into the second term of Eq. (B1), expanding triple cross products, and exploiting the fact that $\mathbf{m} \cdot \dot{\mathbf{m}} = 0$ yields

$$\dot{\mathbf{m}} = \mathbb{L} \mathbf{h}_{\text{eff}} - \frac{\gamma_0 M_s \sigma V}{1 + \alpha^2} \left[\frac{\alpha \mathbf{m} \times \hat{\mathbf{m}}_p - \mathbf{m} \times \mathbf{m} \times \hat{\mathbf{m}}_p}{1 + \nu \mathbf{m} \cdot \hat{\mathbf{m}}_p} \right]. \quad (\text{B2})$$

Because α is of order 10^{-2} , the α^2 term in the denominator is usually dropped. In our case, this is not necessary.

Because the first term in brackets is proportional to α it has been named the ‘‘damping-like’’ torque, and the second term the ‘‘field-like’’ torque. This is unfortunate since the second term acts along the field lines while first term is curl-like. Following our discussion about thermal equilibrium it should be clear that the second term permits the definition of a potential, while the first does not. In our framework, the first term gets absorbed by the transformation to the rotating frame while the second term is absorbed into the energy functional.

In standard micromagnetic packages [39,61] the third term in Eq. (B1) is written as

$$|\gamma_0| \beta \epsilon (\mathbf{m} \times \mathbf{m}_p \times \mathbf{m}), \quad (\text{B3})$$

with the parameters

$$\epsilon = \frac{P \Lambda^2}{(\Lambda^2 + 1) + (\Lambda^2 - 1)(\mathbf{m} \cdot \mathbf{m}_p)} \quad \text{and} \quad \beta = \left| \frac{\hbar}{\mu_0 e} \right| \frac{J}{d M_s}$$

with polarization P , asymmetry Λ , and current density J expressed in units of A/m^2 . The parameters ν and Λ are related by

$$\nu = \frac{\Lambda^2 - 1}{\Lambda^2 + 1}, \quad \Lambda^2 = \frac{1 + \nu}{1 - \nu}.$$

The normalized spin-torque coefficient is $\sigma = \frac{J}{J_c}$, where the critical current density $J_c = \frac{\mu_0 e d M_s^2}{\xi \hbar}$ depends on an efficiency factor $\xi = \frac{P(\nu+1)}{2}$ which in this paper we fixed to $\xi = 1$.

APPENDIX C: EQUILIBRIUM DISTRIBUTION OF THE LANDAU-LIFSHITZ AND LANDAU-LIFSHITZ-GILBERT EQUATIONS

In this section we summarize the well known result that dynamical systems of the form Eq. (21) evolve toward a thermal equilibrium distribution for the magnetization. Consider a segment $dV = l_{\text{ex}}^2 d$ of the sample with uniform magnetization; the exchange interaction with nearest-neighbor regions can be assumed to be included in the effective field. In this section we assume that the restrictions described above are satisfied.

To study thermal effects we separate the stochastic field \mathbf{h}_{th} from the deterministic field $\mathbf{h}_{\text{det}} = \mathbf{h}_{\text{eff}} + \mathbf{h}_{\text{ST}}$. In this way, Eq. (21) can be written in Langevin form as [40]

$$\dot{\mathbf{m}}_{\text{rotating frame}} = \mathbb{L} \mathbf{h}_{\text{det}} + \mathbb{L} \mathbf{h}_{\text{th}} \quad (\text{C1})$$

which, due to the constraint of constant magnetization magnitude, can be interpreted using either the Ito or Stratonovich interpretation [41].

For the following discussion it is convenient to rescale the energy functional $\mathcal{E}' = -\frac{\mathcal{E}_{\text{tot}}}{\mu_0 M_s^2}$ and rewrite the deterministic field as $\mathbf{h}_{\text{det}} = -\frac{\delta \mathcal{E}'_{\text{tot}}}{\delta \mathbf{m}}$. The standard way of writing the RHS of Eq. (C1) is as the sum of a ‘‘deterministic drift,’’ representing the evolution at zero temperature, $\mathbf{b} = \mathbb{L} \mathbf{h}_{\text{det}}$, and a stochastic noise process $\mathbf{h}_{\text{th}} = \sqrt{2\eta} \dot{\mathbf{W}}$:

$$\dot{\mathbf{m}}_{\text{rotating frame}} = \mathbf{b} + \sqrt{2\eta} \mathbb{L} \dot{\mathbf{W}}. \quad (\text{C2})$$

In the jargon of stochastic equations \mathbb{L} is known as the diffusion matrix, and the product $a = \mathbb{L} \mathbb{L}^T$ as the diffusion tensor.

The diffusion matrix can be separated into a symmetric and antisymmetric part:

$$\mathbb{L} = \mathbb{L}_{\mathbb{S}} + \mathbb{L}_{\mathbb{A}}. \quad (\text{C3})$$

Conveniently, the two parts satisfy $\mathbb{L}_{\mathbb{A}} \mathbb{L}_{\mathbb{A}}^T = -\frac{\gamma' M_s}{\alpha} \mathbb{L}_{\mathbb{S}}$. This is seen more easily using tensor notation:

$$\mathbb{L}_{\mathbb{A}_{i,k}} = -\gamma' M_s \epsilon_{ijk} m_j, \quad (\text{C4})$$

$$\mathbb{L}_{\mathbb{S}_{i,k}} = \gamma' M_s \alpha [\delta_{i,k} - m_i m_k]. \quad (\text{C5})$$

Using the property of the Levi-Civita tensor $\epsilon_{ijk} \epsilon_{imn} = (\delta_{jm} \delta_{kn} - \delta_{jn} \delta_{km})$, the diffusion tensor and its ‘‘inverse’’ can be shown to be, respectively,

$$a = \gamma'^2 M_s^2 (1 + \alpha^2) [\delta_{i,k} - m_i m_k] = \frac{\gamma_0}{\alpha} M_s \mathbb{L}_{\mathbb{S}}, \quad (\text{C6})$$

$$a^{-1} = \frac{[\delta_{i,k} - m_i m_k]}{\gamma'^2 M_s^2 (1 + \alpha^2)}. \quad (\text{C7})$$

Because the diffusion tensor has a zero eigenvalue, it is not invertible. As a consequence, the component of the thermal field parallel to \mathbf{m} has no effect on the time evolution, and its inverse is defined only for vectors perpendicular to \mathbf{m} , which is the case for both $\dot{\mathbf{m}}$ and \mathbf{b} . For this reason, the noninvertibility of a in three dimensions presents no obstacle for analysis.

The analysis presented in [40] shows that the Langevin-type Eq. (C2) is associated with a Fokker-Planck

equation of the form

$$\dot{P} = \nabla_{\mathbf{m}} \cdot ([\mathbf{b} - \eta \mathbb{L} \mathbb{L}^T \nabla_{\mathbf{m}}] P). \quad (\text{C8})$$

For the noise strength η to be directly related to temperature, the Boltzmann distribution $P(\mathbf{m}) = \frac{1}{Z} e^{-\frac{\mathcal{E}_{\text{tot}} d\mathcal{V}}{k_B T}}$ must be a stationary solution of the Fokker-Planck equation; i.e.,

$$\dot{P} = \nabla_{\mathbf{m}} \cdot \left([\mathbf{b} - \eta \mathbb{L} \mathbb{L}^T \nabla_{\mathbf{m}}] \frac{1}{Z} e^{-\frac{\mathcal{E}_{\text{tot}} d\mathcal{V}}{k_B T}} \right) \quad (\text{C9})$$

must vanish.

To proceed, it is useful to write \mathbf{b} as

$$\mathbf{b} = (\mathbb{L}_S + \mathbb{L}_A) \left(-\frac{\delta \mathcal{E}'_{\text{tot}}}{\delta \mathbf{m}} \right). \quad (\text{C10})$$

The antisymmetric parts result in a curl-like term,

$$\begin{aligned} \mathbb{L}_A \left(-\frac{\delta \mathcal{E}'_{\text{tot}}}{\delta \mathbf{m}} \right) P &= \gamma' M_s \mathbf{m} \times \frac{\delta \mathcal{E}'_{\text{tot}}}{\delta \mathbf{m}} \frac{1}{Z} e^{-\frac{\mathcal{E}_{\text{tot}}}{k_B T}} \\ &= \frac{\gamma'}{\mu_0 M_s} \nabla_{\mathbf{m}} \times (\mathbf{m} \mathcal{E}'_{\text{tot}}) \frac{1}{Z} e^{-\frac{\mathcal{E}_{\text{tot}}}{k_B T}} \\ &= -\frac{\gamma' k_B T}{\mu_0 M_s d \mathcal{V}} \nabla_{\mathbf{m}} \times (\mathbf{m} P), \end{aligned} \quad (\text{C11})$$

which is divergenceless. In a similar fashion, the symmetric piece becomes gradient-like:

$$\begin{aligned} P \mathbb{L}_S \left(-\frac{\delta \mathcal{E}'_{\text{tot}}}{\delta \mathbf{m}} \right) &= -\mathbb{L}_S \frac{1}{Z} e^{-\frac{\mathcal{E}_{\text{tot}}}{k_B T}} \nabla_{\mathbf{m}} \mathcal{E}'_{\text{tot}} \\ &= \frac{k_B T}{\mu_0 M_s^2 d \mathcal{V}} \mathbb{L}_S \nabla_{\mathbf{m}} P. \end{aligned} \quad (\text{C12})$$

The stationarity condition, $\dot{P} = 0$, can be simplified as

$$\begin{aligned} 0 &= \nabla_{\mathbf{m}} \cdot \left(\frac{k_B T \mathbb{L}_S \nabla_{\mathbf{m}} P}{\mu_0 M_s^2 d \mathcal{V}} - \frac{\eta \gamma_0 M_s \mathbb{L}_S \nabla_{\mathbf{m}} P}{\alpha} \right) \\ &= \nabla_{\mathbf{m}} \cdot \left(\left[\frac{k_B T}{\mu_0 M_s^2 d \mathcal{V}} - \frac{\eta \gamma_0 M_s}{\alpha} \right] \mathbb{L}_S \nabla_{\mathbf{m}} P \right). \end{aligned} \quad (\text{C13})$$

This establishes the relation between the noise strength and temperature as $\eta = \frac{\alpha k_B T}{2Ad\gamma_0 M_s}$. We emphasize that the second term in Eq. (19) is the reason that most spin-torque-driven systems are not in thermal equilibrium.

In the stationary reference frame, the Fokker-Planck equation leads to a differential equation for the distribution P of the form

$$\dot{P} = \nabla_{\mathbf{m}} \cdot \left(-\frac{\gamma_0}{\mu_0 M_s} \nabla_{\mathbf{m}} \times (\mathbf{m} \mathcal{E}_{\text{ST}}) P \right) \quad (\text{C14})$$

since all other terms on the RHS still cancel. This can be manipulated into the more compact form

$$\dot{P} = -P \frac{2Ad\gamma_0 M_s}{k_B T} \Xi = -P \frac{\alpha}{\eta} \Xi, \quad (\text{C15})$$

which implies that fluctuations near equilibrium evolve at a rate $\frac{\alpha}{\eta} \Xi$.

APPENDIX D: UNIAXIAL MACROSPIN

Previous work (see, for example, [37,62–64]) has studied the problem of reversal rates of a uniaxial macrospin in the

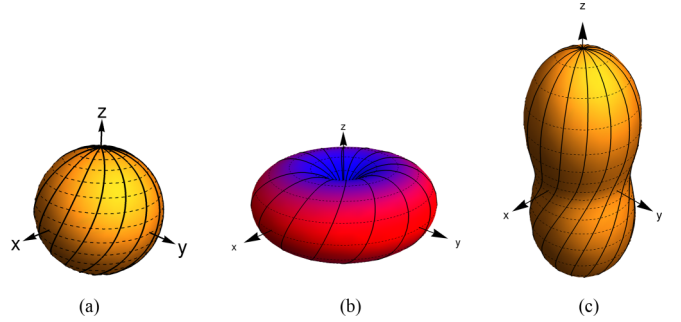


FIG. 12. (a) Instantaneous state of a twisted coordinate system produced by a latitude-dependent rate of rotation. (b) The hypothetical energy surface of a system with rotational symmetry sharing the polar axis with the twisting coordinate system. The shape of this surface remains unchanged even though the coordinate system is twisted around it. (c) The corresponding Boltzmann distribution function for the same magnetic system at a high temperature.

presence of STT. Here, we briefly discuss how our approach compares to previous work on these systems.

References [62–64] introduce an effective energy term as an ansatz for the stationary solution of the Fokker-Planck equation; this term is consistent with our definition of the pseudoenergy. The equations of motion are phenomenologically equivalent, but our version has an explicit curl-like term. As explained in the main text, this term can be absorbed by transforming to an appropriate reference frame when $\nu = 0$.

However, when $\nu \neq 0$, one cannot drop the second term of Eq. (18). Nevertheless, in the highly symmetric case such a term does not result in an increase of the total energy \mathcal{E}_{tot} . Its inclusion in the dynamics affects the *deterministic* trajectories but not the energy distribution of the ensemble. For this reason, the Boltzmann distribution for $\nu = 0$ is also a solution of the Fokker-Planck equation when $\nu \neq 0$ as long as the fields are axially symmetric.

A simple geometrical analog helps clarify this point. In a spherical coordinate system with $\hat{\mathbf{m}}_p$ as the polar axis, $\mathbf{m} \cdot \mathbf{h}_{\text{ST}} = \cos \Theta$, $\mathbf{m} \times \hat{\mathbf{m}}_p = -\sin \Theta \hat{\Phi}$, and the second term in Eq. (18) becomes

$$-\nu [\mathbf{m} \cdot \mathbf{h}_{\text{ST}}] \mathbf{m} \times \hat{\mathbf{m}}_p = \omega(\nu; \Theta) \sin \Theta \hat{\Phi}$$

with

$$\omega(\nu; \Theta) = \omega_{\text{ST}} \frac{\nu \cos \Theta}{(1 + \nu \cos \Theta)}.$$

This would have the proper structure except that now the angular velocity of the rotating frame depends on Θ . In that case, one could envision a twisted coordinate systems for which the meridians twist around $\hat{\mathbf{m}}_p$ in a screw-like fashion, such as the one shown in Fig. 12(a), with the degree of twist increasing with time. With the exception of the poles, the transformation between a fixed frame and a twisting reference frame is invertible. Because none of the energy terms depend on the azimuthal angle, the energy remains unchanged even as the meridians appear more twisted from the perspective of the stationary frame [Fig. 1(b)]. In consequence, the equilibrium distribution function is invariant even though the individual trajectories of the particle become more mixed.

In summary, the introduction of a pseudoenergy associated with spin torque, the absorption of the extra precessional term into a change of reference frame, and the symmetry of the pseudoenergy with respect to the reference frame guarantee that at long times uniaxially symmetric systems reach thermal equilibrium in the presence of spin torque even for cases where $\nu \neq 0$.

The work of Pinna *et al.* [37] treats the uniaxial problem using the Freidlin-Wentzell formalism. Their fluctuational trajectories are the macrospin version of the fluctuational trajectories proposed in Sec. IX. They demonstrated that, provided the deviation from uniaxial symmetry is not too strong, the fluctuational paths will not cross and the optimal escape trajectory remains well behaved (e.g., no singularities occur in the action). As shown in Sec. IX, the action along the escape fluctuational path remains $S = 2\Delta\mathcal{E}_{\text{tot}}$.

Because of its symmetry, the uniaxial macrospin case provides a simpler situation which shows that these two distinct approaches provide consistent and complementary results.

APPENDIX E: EXPLICIT EXPRESSIONS FOR ENERGY AND FIELD IN THE ROTATING FRAME

The pseudoenergy used in this paper is given by $\mathcal{E}_{\text{tot}} = \mathcal{E}_{\text{ex}} + \mathcal{E}_K + \mathcal{E}_Z + \mathcal{E}_{\text{ST}}$. Although the pseudoenergy is invariant under changes of reference frame, the explicit form of all terms (except \mathcal{E}_{ex}) depends on the orientation of the coordinate axes. The fields in the rotating frame can be obtained using the general expressions

$$h_{\Theta} = -\frac{1}{\mu_0 M_s^2} \frac{\delta \mathcal{E}}{\delta \Theta}, \quad h_{\Phi} = -\frac{1}{\mu_0 M_s^2} \frac{1}{\sin \Theta} \frac{\delta \mathcal{E}}{\delta \Phi}. \quad (\text{E1})$$

Following [25], we will treat Φ and Θ perturbatively with the expansions

$$\Theta = \Theta_0 + \epsilon \Theta_1, \quad \Phi = \Phi_0 + \frac{\epsilon \Phi_1}{\sin \Theta_0}. \quad (\text{E2})$$

Here Θ_0 and $\Phi_0 = 0$ are solutions of Eqs. (24) and (25) with ϵ set to zero; Θ_1 and Φ_1 are the perturbative solutions to first order in ϵ . The expansion incorporates perturbations arising from small experimental misalignments θ_z , θ_f and the spin-torque asymmetry parameter ν . To denote the order of the perturbation we use a superscript; e.g., $h_{\text{ex},\Phi}^{(1)}$ denotes the perturbation expansion to first order in the exchange-induced field in the azimuthal direction.

To first order, the azimuthal time derivative is

$$\sin \Theta \dot{\Phi} \approx (\sin \Theta \dot{\Phi})^{(0)} + \epsilon \Theta_1 \cos \Theta_0 \dot{\Phi}_0 + \epsilon \dot{\Phi}_1. \quad (\text{E3})$$

We now consider the contributions of each of the terms in the pseudoenergy.

1. Exchange

The exchange energy surface density is invariant with respect to changes in the coordinate system,

$$\frac{\mathcal{E}_{\text{ex}}}{\mu_0 M_s^2} = \frac{l_{\text{ex}}^2}{2} (|\nabla \Theta|^2 + \sin^2 \Theta |\nabla \Phi|^2). \quad (\text{E4})$$

Similarly for the field expressions,

$$h_{\text{ex},\Phi} = \sin \Theta \nabla^2 \Phi + 2 \cos \Theta \nabla \Theta \cdot \nabla \Phi, \quad (\text{E5})$$

$$h_{\text{ex},\Theta} = \nabla^2 \Theta - \frac{1}{2} \sin 2\Theta |\nabla \Phi|^2. \quad (\text{E6})$$

Their perturbative expansions, to first order in ϵ , are

$$h_{\text{ex},\Phi} \approx \epsilon \left[\nabla^2 \Phi_1 + \Phi_1 (\nabla \Theta_0)^2 - \Phi_1 \frac{\cos \Theta_0}{\sin \Theta_0} \nabla^2 \Theta_0 \right] \quad (\text{E7})$$

and

$$h_{\text{ex},\Theta} \approx h_{\text{ex},\Theta}^{(0)} + \epsilon [\nabla^2 \Theta_1], \quad (\text{E8})$$

where $h_{\text{ex},\Theta}^{(0)} = \nabla^2 \Theta_0$. We note that the term in square brackets with $\sin \Theta_0$ in the denominator can be replaced by using the equation for $h_{\Theta}^{(0)} = 0$ [Eq. (51)]. The first-order term is then

$$h_{\text{ex},\Phi}^{(1)} \approx \{[(\nabla \Theta_0)^2 - \cos \Theta_0 (\cos \Theta_0 - \omega_h)] + \nabla^2\} \Phi_1. \quad (\text{E9})$$

2. Anisotropy

The anisotropy surface energy density

$$\frac{\mathcal{E}_K}{\mu_0 M_s^2} = -\frac{Q-1}{2} (\mathbf{m} \cdot \hat{\mathbf{z}}_L)^2 \quad (\text{E10})$$

favors magnetization orientation along the anisotropy axis $\hat{\mathbf{z}}_L$, which is oriented perpendicular to the sample plane. This axis rotates around $\hat{\mathbf{m}}_p$ in the rotating frame. These two vectors make an angle θ_f . The energy density for a given magnetization orientation (Θ, Φ) in the rotating frame is time dependent:

$$\frac{\mathcal{E}_K}{\mu_0 M_s^2} = -\frac{[\sin \Theta \sin \theta_f \cos(\omega t + \Phi) + \cos \theta_f \cos \Theta]^2}{2/(Q-1)}. \quad (\text{E11})$$

Consequently, the fields are

$$\begin{aligned} \frac{h_{K,\Theta}}{Q-1} &= \frac{1}{2} \sin 2\Theta \sin^2 \theta_f \cos^2(\omega t + \Phi) \\ &+ \frac{1}{4} \cos 2\Theta \sin 2\theta_f \cos(\omega t + \Phi) \\ &- \frac{1}{2} \sin 2\Theta \cos^2 \theta_f \end{aligned} \quad (\text{E12})$$

and

$$\begin{aligned} \frac{h_{K,\Phi}}{Q-1} &= -\frac{1}{2} \sin \Theta \sin^2 \theta_f \sin[2(\omega t + \Phi)] \\ &- \frac{1}{2} \cos \Theta \sin 2\theta_f \sin(\omega t + \Phi). \end{aligned} \quad (\text{E13})$$

We set $h_{K,\Theta}^{(0)} = \frac{Q-1}{2} \sin 2\Theta_0$ for the limit $\theta_f = 0$. The perturbative expansions for small θ_f are

$$\begin{aligned} \frac{h_{K,\Theta}}{Q-1} &\approx \frac{h_{K,\Theta}^{(0)}}{Q-1} \\ &- \frac{\theta_f}{2} \cos 2\Theta_0 \cos \omega t + \epsilon \Theta_1 \cos 2\Theta_0 \end{aligned} \quad (\text{E14})$$

and

$$h_{K,\Phi} \approx \frac{1}{2} (Q-1) \theta_f \cos \Theta_0 \sin \omega t. \quad (\text{E15})$$

3. Zeeman

To describe the orientation of the field, we use polar coordinates in the laboratory reference frame,

$$\mathbf{h}_Z = (\cos \phi_Z \sin \theta_Z, \sin \phi_Z \sin \theta_Z, \cos \theta_Z), \quad (\text{E16})$$

where the field misalignment θ_z is presumed to be small. The Zeeman energy density $\frac{\mathcal{E}_Z}{\mu_0 M_s^2} = -\mathbf{m} \cdot \mathbf{h}_Z$ in the rotating frame is

$$\begin{aligned} \frac{\mathcal{E}_Z}{-h_Z \mu_0 M_s^2} &= \cos \phi_Z \sin \theta_z [\sin \Theta \cos \theta_f \cos(\omega t + \Phi) \\ &\quad - \sin \theta_f \cos \Theta] \sin \phi_Z \sin \theta_z \sin \Theta \sin(\omega t + \Phi) \\ &\quad + \cos \theta_z [\sin \Theta \sin \theta_f \cos(\omega t + \Phi) \\ &\quad + \cos \theta_f \cos \Theta], \end{aligned} \quad (\text{E17})$$

with corresponding fields

$$\begin{aligned} \frac{h_{Z,\Theta}}{h_Z} &= \cos \phi_Z \sin \theta_z [\cos \Theta \cos \theta_f \cos(\omega t + \Phi) \\ &\quad + \sin \theta_f \sin \Theta] \sin \phi_Z \sin \theta_z \cos \Theta \sin(\omega t + \Phi) \\ &\quad + \cos \theta_z [\cos \Theta \sin \theta_f \cos(\omega t + \Phi) - \cos \theta_f \sin \Theta] \end{aligned} \quad (\text{E18})$$

and

$$\begin{aligned} \frac{h_{Z,\Phi}}{h_Z} &= -\cos \phi_Z \sin \theta_z \cos \theta_f \sin(\omega t + \Phi) \\ &\quad + \sin \phi_Z \sin \theta_z \cos(\omega t + \Phi) \\ &\quad - \cos \theta_z \sin \theta_f \sin(\omega t + \Phi). \end{aligned} \quad (\text{E19})$$

Using $h_{Z,\Theta}^{(0)} = -\sin \Theta_0$, the leading-order perturbation expansions for small θ_z and θ_f are

$$\begin{aligned} \frac{h_{Z,\Theta}}{h_Z} &= h_{Z,\Theta}^{(0)} + \theta_z \cos \Theta_0 \cos(\omega t - \phi_Z) \\ &\quad + \theta_f \cos \Theta \cos(\omega t) - \epsilon \Theta_1 \cos \Theta_0 \end{aligned} \quad (\text{E20})$$

and

$$\frac{h_{Z,\Phi}}{h_Z} = -\theta_z \cos \phi_Z \sin(\omega t - \phi_z) - \theta_f \sin(\omega t). \quad (\text{E21})$$

4. Spin torque

The pseudopotential energy density and field were introduced in Eqs. (16) and (17). The denominator of the spin-torque field term can be written as an expansion in ν :

$$\frac{1}{1 + \nu \mathbf{m} \cdot \hat{\mathbf{m}}_p} = \sum_{n=0}^{\infty} (-\nu \mathbf{m} \cdot \hat{\mathbf{p}})^n. \quad (\text{E22})$$

Notice that in the rotating frame $\mathbf{m} \cdot \hat{\mathbf{m}}_p = \cos \Theta$, $\hat{\mathbf{m}}_p \cdot \hat{\Theta} = -\sin \Theta$, and $\hat{\mathbf{m}}_p \cdot \hat{\Phi} = 0$. After rescaling, the field components are

$$h_{\text{ST},\Theta} = +\frac{\sigma V}{\alpha} \sin \Theta \sum_{n=0}^{\infty} (-\nu \cos \Theta)^n \quad (\text{E23})$$

and

$$h_{\text{ST},\Phi} = 0. \quad (\text{E24})$$

Taking ν as a small parameter and $h_{\text{ST},\Theta}^{(0)} = \frac{\sigma V}{\alpha} \sin \Theta_0$, the perturbative expansion becomes

$$h_{\text{ST},\Theta} = h_{\text{ST},\Theta}^{(0)} + \frac{\sigma V}{\alpha} \left[\epsilon \Theta_1 \cos \Theta_0 - \frac{\nu}{2} \sin 2\Theta_0 \right]. \quad (\text{E25})$$

To first order in ν , the term in parentheses in Eq. (25) is

$$\frac{\sigma' V}{\alpha' \Theta} - \sin \Theta \approx -\nu \frac{\sigma' V}{2\alpha'} \sin 2\Theta_0. \quad (\text{E26})$$

-
- [1] A. M. Kosevich, B. A. Ivanov, and A. S. Kovalev, Magnetic solitons, *Phys. Rep.* **194**, 117 (1990).
- [2] T. Chen, R. K. Dumas, A. Eklund, P. K. Muduli, A. Houshang, A. A. Awad, P. Dürrenfeld, B. G. Malm, A. Rusu, and J. Åkerman, Spin-torque and spin-Hall nano-oscillators, *Proc. IEEE* **104**, 1919 (2016).
- [3] F. Macià, D. Backes, and A. D. Kent, Stable magnetic droplet solitons in spin-transfer nanocontacts, *Nat. Nanotechnol.* **9**, 992 (2014).
- [4] B. Divinskiy, S. Urazhdin, V. E. Demidov, A. Kozhanov, A. P. Nosov, A. B. Rinkevich, and S. O. Demokritov, Magnetic droplet solitons generated by pure spin currents, *Phys. Rev. B* **96**, 224419 (2017).
- [5] Y. Zhou, E. Iacocca, A. A. Awad, R. K. Dumas, F. C. Zhang, H. B. Braun, and J. Åkerman, Dynamically stabilized magnetic skyrmions, *Nat. Commun.* **6**, 8193 (2015).
- [6] B. A. Ivanov and A. M. Kosevich, Bound states of a large number of magnons in a ferromagnet with single ion anisotropy, *Zh. Eksp. Teor. Fiz.* **72**, 2000 (1977) [*Sov. Phys. JETP* **45**, 1050 (1977)].
- [7] V. G. Makhankov, Dynamics of classical solitons (in non-integrable systems), *Phys. Rep.* **35**, 1 (1978).
- [8] S. M. Mohseni, S. R. Sani, J. Persson, T. N. A. Nguyen, S. Chung, Y. Pogoryelov, P. K. Muduli, E. Iacocca, A. Eklund, R. K. Dumas, S. Bonetti, A. Deac, M. A. Hofer, and J. Åkerman, Spin torque-generated magnetic droplet solitons, *Science* **339**, 1295 (2013).
- [9] D. Backes, F. Macià, S. Bonetti, R. Kukreja, H. Ohldag, and A. D. Kent, Direct Observation of a Localized Magnetic Soliton in a Spin-Transfer Nanocontact, *Phys. Rev. Lett.* **115**, 127205 (2015).
- [10] J. Hang, C. Hahn, N. Statuto, F. Macià, and A. D. Kent, Generation and annihilation time of magnetic droplet solitons, *Sci. Rep.* **8**, 6847 (2018).
- [11] S. Chung, Q. T. Le, M. Ahlberg, A. A. Awad, M. Weigand, I. Bykova, R. Khymyn, M. Dvornik, H. Mazraati, A. Houshang, S. Jiang, T. N. A. Nguyen, E. Goering, G. Schütz, J. Gräfe, and

- J. Åkerman, Direct Observation of Zhang-Li Torque Expansion of Magnetic Droplet Solitons, *Phys. Rev. Lett.* **120**, 217204 (2018).
- [12] O. R. Sulymenko, O. V. Prokopenko, V. S. Tyberkevych, A. N. Slavin, and A. A. Serga, Bullets and droplets: Two-dimensional spin-wave solitons in modern magnonics, *J. Low Temp. Phys.* **44**, 602 (2018).
- [13] E. Iacocca, R. K. Dumas, L. Bookman, M. Mohseni, S. Chung, M. A. Hofer, and J. Åkerman, Confined Dissipative Droplet Solitons in Spin-Valve Nanowires with Perpendicular Magnetic Anisotropy, *Phys. Rev. Lett.* **112**, 047201 (2014).
- [14] D. Xiao, Y. Liu, Y. Zhou, S. M. Mohseni, S. Chung, and J. Åkerman, Merging droplets in double nanocontact spin torque oscillators, *Phys. Rev. B* **93**, 094431 (2016).
- [15] D. Xiao, V. Tiberkevich, Y. H. Liu, Y. W. Liu, S. M. Mohseni, S. Chung, M. Ahlberg, A. N. Slavin, J. Åkerman, and Y. Zhou, Parametric autoexcitation of magnetic droplet soliton perimeter modes, *Phys. Rev. B* **95**, 024106 (2017).
- [16] M. Mohseni, M. Hamdi, H. F. Yazdi, S. A. H. Banuazizi, S. Chung, S. R. Sani, J. Åkerman, and M. Mohseni, Magnetic droplet soliton nucleation in oblique fields, *Phys. Rev. B* **97**, 184402 (2018).
- [17] S. Jiang, S. Chung, Q. T. Le, H. Mazraati, A. Houshang, and J. Åkerman, Using Magnetic Droplet Nucleation to Determine the Spin Torque Efficiency and Asymmetry in $\text{Co}_x(\text{Ni,Fe})_{1-x}$ Thin Films, *Phys. Rev. Appl.* **10**, 054014 (2018).
- [18] S. Jiang, S. Ruhollah Etesami, S. Chung, Q. T. Le, A. Houshang, and J. Åkerman, Impact of the Oersted field on droplet nucleation boundaries, *IEEE Magn. Lett.* **9**, 3104304 (2018).
- [19] N. Statuto, C. Hahn, J. M. Hernández, A. D. Kent, and F. Macià, Multiple magnetic droplet soliton modes, *Phys. Rev. B* **99**, 174436 (2019).
- [20] M. Mohseni, Q. Wang, M. Mohseni, T. Brächer, B. Hillebrands, and P. Pirro, Propagating Magnetic Droplet Solitons as Moveable Nanoscale Spin-Wave Sources with Tunable Direction of Emission, *Phys. Rev. Appl.* **13**, 024040 (2020).
- [21] M. Mohseni, D. R. Rodrigues, M. Saghafi, S. Chung, M. Ahlberg, H. F. Yazdi, Q. Wang, S. A. H. Banuazizi, P. Pirro, J. Åkerman, and M. Mohseni, Chiral excitations of magnetic droplet solitons driven by their own inertia, *Phys. Rev. B* **101**, 020417(R) (2020).
- [22] J. C. Slonczewski, Current-driven excitation of magnetic multilayers, *J. Magn. Magn. Mater.* **159**, L1 (1996).
- [23] L. Berger, Emission of spin waves by a magnetic multilayer traversed by a current, *Phys. Rev. B* **54**, 9353 (1996).
- [24] L. D. Bookman and M. A. Hofer, Analytic theory of modulated magnetic solitons, *Phys. Rev. B* **88**, 184401 (2013).
- [25] M. A. Hofer, T. J. Silva, and M. W. Keller, Theory for a dissipative droplet soliton excited by a spin torque nanocontact, *Phys. Rev. B* **82**, 054432 (2010).
- [26] P. Wills, E. Iacocca, and M. A. Hofer, Deterministic drift instability and stochastic thermal perturbations of magnetic dissipative droplet solitons, *Phys. Rev. B* **93**, 144408 (2016).
- [27] R. O. Moore and M. A. Hofer, Stochastic ejection of nanocontact droplet solitons via drift instability, *Phys. Rev. B* **100**, 014402 (2019).
- [28] S. Lendínez, N. Statuto, D. Backes, A. D. Kent, and F. Macià, Observation of droplet soliton drift resonances in a spin-transfer-torque nanocontact to a ferromagnetic thin film, *Phys. Rev. B* **92**, 174426 (2015).
- [29] P. Hänggi, P. Talkner, and M. Borkovec, Reaction-rate theory: Fifty years after Kramers, *Rev. Mod. Phys.* **62**, 251 (1990).
- [30] M. I. Freidlin and A. D. Wentzell, *Random Perturbations of Dynamical Systems*, 3rd ed. (Springer, Berlin, 2012).
- [31] B. J. Matkowsky and Z. Schuss, On the lifetime of a metastable state at low noise, *Phys. Lett. A* **95**, 213 (1983).
- [32] R. S. Maier and D. L. Stein, Escape problem for irreversible systems, *Phys. Rev. E* **48**, 931 (1993).
- [33] W. F. Brown, Jr., Thermal fluctuations of a single-domain particle, *Phys. Rev.* **130**, 1677 (1963).
- [34] H.-B. Braun, Thermally Activated Magnetic Reversal in Elongated Ferromagnetic Particles, *Phys. Rev. Lett.* **71**, 3557 (1993).
- [35] Weinan E., W. Ren, and E. vanden Eijnden, String method for the study of rare events, *J. Appl. Phys.* **93**, 2275 (2003).
- [36] K. Martens, D. L. Stein, and A. D. Kent, Magnetic reversal in nanoscopic ferromagnetic rings, *Phys. Rev. B* **73**, 054413 (2006).
- [37] D. Pinna, A. D. Kent, and D. L. Stein, Large fluctuations and singular behavior of nonequilibrium systems, *Phys. Rev. E* **93**, 012114 (2016).
- [38] R. Graham and T. Tél, Nonequilibrium potential for coexisting attractors, *Phys. Rev. A* **33**, 1322 (1986).
- [39] M. J. Donahue and D. G. Porter, OOMMF user's guide, version 1.0, Interagency Report NISTIR 6376, National Institute of Standards and Technology, Gaithersburg, MD, 1999.
- [40] J. L. García-Palacios and F. J. Lázaro, Langevin-dynamics study of the dynamical properties of small magnetic particles, *Phys. Rev. B* **58**, 14937 (1998).
- [41] D. V. Berkov, Magnetization dynamics including thermal fluctuations: Basic phenomenology, fast remagnetization processes and transitions over high-energy barriers, *Handbook of Magnetism and Advanced Magnetic Materials* (American Cancer Society, Hoboken, NJ, 2007).
- [42] G. Bertotti, I. D. Mayergoyz, and C. Serpico, Nonlinear magnetization dynamics: Switching and relaxation phenomena, *The Science of Hysteresis*, Vol. 2 (Elsevier, Cambridge, UK, 2006), pp. 435–565.
- [43] See Supplemental Material at <http://link.aps.org/supplemental/10.1103/PhysRevB.101.184421> for the source code used in the different parts of this paper.
- [44] C. Serpico, G. Bertotti, I. D. Mayergoyz, and M. d'Aquino, Nonlinear magnetization dynamics in nanomagnets, *Handbook of Magnetism and Advanced Magnetic Materials* (American Cancer Society, Hoboken, NJ, 2007).
- [45] R. S. Wedemann, A. R. Plastino, and C. Tsallis, Curl forces and the nonlinear Fokker-Planck equation, *Phys. Rev. E* **94**, 062105 (2016).
- [46] M. V. Berry and P. Shukla, Curl force dynamics: Symmetries, chaos and constants of motion, *New J. Phys.* **18**, 063018 (2016).
- [47] M. V. Berry and P. Shukla, Hamiltonian curl forces, *Proc. R. Soc. A* **471**, 20150002 (2015).
- [48] K. A. Newhall and E. Vanden-Eijnden, Averaged equation for energy diffusion on a graph reveals bifurcation diagram and thermally assisted reversal times in spin-torque driven nanomagnets, *J. Appl. Phys.* **113**, 184105 (2013).

- [49] D. Pinna, A. D. Kent, and D. L. Stein, Thermally assisted spin-transfer torque dynamics in energy space, *Phys. Rev. B* **88**, 104405 (2013).
- [50] W. H. Rippard, A. M. Deac, M. R. Pufall, J. M. Shaw, M. W. Keller, S. E. Russek, G. E. W. Bauer, and C. Serpico, Spin-transfer dynamics in spin valves with out-of-plane magnetized CoNi free layers, *Phys. Rev. B* **81**, 014426 (2010).
- [51] S. M. Mohseni, S. R. Sani, J. Persson, T. N. Anh Nguyen, S. Chung, Y. Pogoryelov, and J. Åkerman, High frequency operation of a spin-torque oscillator at low field, *Phys. Status Solidi RRL* **5**, 432 (2011).
- [52] J. Xiao, A. Zangwill, and M. D. Stiles, Boltzmann test of Slonczewski's theory of spin-transfer torque, *Phys. Rev. B* **70**, 172405 (2004).
- [53] M. A. Hofer, T. J. Silva, and M. D. Stiles, Model for a collimated spin-wave beam generated by a single-layer spin torque nanocontact, *Phys. Rev. B* **77**, 144401 (2008).
- [54] L. D. Bookman and M. A. Hofer, Perturbation theory for propagating magnetic droplet solitons, *Proc. R. Soc. A* **471**, 20150042 (2015).
- [55] S. Chung, A. Eklund, E. Iacocca, S. M. Mohseni, S. R. Sani, L. Bookman, M. A. Hofer, R. K. Dumas, and J. Åkerman, Magnetic droplet nucleation boundary in orthogonal spin-torque nano-oscillators, *Nat. Commun.* **7**, 11209 (2016).
- [56] S. Lendínez, J. Hang, S. Vélez, J. M. Hernández, D. Backes, A. D. Kent, and F. Macià, Effect of Temperature on Magnetic Solitons Induced by Spin-Transfer Torque, *Phys. Rev. Appl.* **7**, 054027 (2017).
- [57] R. V. Kohn and V. V. Slastikov, Another thin-film limit of micromagnetics, *Arch. Rat. Mech. Anal.* **178**, 227 (2005).
- [58] J. E. Miltat and M. J. Donahue, Numerical micromagnetics: Finite difference methods, *Handbook of Magnetism and Advanced Magnetic Materials* (American Cancer Society, Hoboken, NJ, 2007).
- [59] N. Statuto, J. M. Hernández, A. D. Kent, and F. Macià, Generation and stability of dynamical skyrmions and droplet solitons, *Nanotechnology* **29**, 325302 (2018).
- [60] D. C. Ralph and M. D. Stiles, Spin transfer torques, *J. Magn. Mater.* **320**, 1190 (2008).
- [61] A. Vansteenkiste, J. Leliaert, M. Dvornik, M. Helsen, F. Garcia-Sanchez, and B. Van Waeyenberge, The design and verification of MuMax3, *AIP Adv.* **4**, 107133 (2014).
- [62] W. H. Butler, T. Mewes, C. K. A. Mewes, P. B. Visscher, W. H. Rippard, S. E. Russek, and R. Heindl, Switching distributions for perpendicular spin-torque devices within the macrospin approximation, *IEEE Trans. Magn.* **48**, 4684 (2012).
- [63] T. Taniguchi and H. Imamura, Thermally assisted spin transfer torque switching in synthetic free layers, *Phys. Rev. B* **83**, 054432 (2011).
- [64] J. He, J. Z. Sun, and S. Zhang, Switching speed distribution of spin-torque-induced magnetic reversal, *J. Appl. Phys.* **101**, 09A501 (2007).